RPNSci

RESEARCH PROSPECTS IN NATURAL SCIENCES

VOLUME 1
ISSUE 1
2023

PUBLISHER
GOVERNMENT GRADUATE COLLEGE, TOWNSHIP, LAHORE

RESEARCH PROSPECTS IN NATURAL SCIENCES

Volume 1; issue 1

Publisher: Government Graduate College, Township, LAHORE

Published by Government Graduate College, Township, Lahore.

Publication Data: December 2023

Research Prospects in Natural Sciences: A Research Journal
Printed in Lahore, Pakistan.

Contents

Available online at www.rpnsci.com

Research Prospects in Natural Sciences Vol. 1, Issue 1, (2023) 1–5

Research Article

Conventional and Microwave-assisted Synthesis of Fibric Acid Based 1,3,4-oxadiazole Derivatives and Evaluation of Their *in vivo* Anti-hyperglycemic Activity

Majda Batool[a,b,*], Munawar Ali Munawar[c], Muhammad Asim Raza Basra[a], Sumra Amanat[b], Shazia Amir[b], Hafiz Adnan Ahmad[b]

[a]*School of Chemistry, University of the Punjab, Lahore 54600, Pakistan*
[b]*Department of Chemistry, Government Graduate College, Township, Lahore 54700, Pakistan.*
[c]*Department of Chemistry, Faculty of Science, University of Central Punjab, Lahore 54700, Pakistan*

Abstract

Microwave assisted synthesis, a green synthetic method was applied to synthesize a series of oxadiazole based fibric acid derivatives **(3a-h)** resulted good to excellent yields (82-96%) and less reaction time in comparison to conventional methods and ultrasonic methods. The synthesized compounds were characterized by ^{1}H-NMR, EI/MS and ^{13}C-NMR and their postulated structures were in agreement with spectral data. In present study title compounds were further evaluated for their hypoglycemic potential and among them compounds **(3c)** showed the significant biological response. The hypoglycemic effect was compared with glibenclamide.

Keywords:
Fiberates, Green chemistry, Microwave, Oxadiazole derivatives, Carboxymethylcellulose, Glibenclamide, Body weight.

1. Introduction

Diabetes mellitus (DM), often referred as simply diabetes, is dysmetabolic syndrome that can have various causes, but is primarily characterized by consistently high blood sugar levels and abnormalities in the metabolism of carbohydrates, proteins, and fats. These abnormalities are typically caused by irregularities in the way insulin works in the body, including both insulin secretion and insulin action. Based on analysis, control and the clinical expressions DM can be classified into many types, each with its own specific causes and aspects. Diabetes type 1, for example, is an immunological disorder in which insulin producing cells are attacked and destroyed by body's immune system. While diabetes type 2, is generally caused by the combination of various genetic and lifestyle factors, that causes insulin resistance, in which body's cells response poorly to insulin. Regardless of the specific cause the end result of diabetes is a chronic state of high blood glucose levels that can lead to a lot of complications if not cared. These can include nerve destruction, kidney disorder, blindness, and an increased risk of cardiovascular disease [1, 2].

Hyperlipidemia and constant high levels of blood glucose are the main common symptoms in almost all the major types of DM [3].The ultimate effects of diabetes mellitus include cut away, retinopathy, cataract and joints disorder. Diabetic patients are also at higher risk of developing heart disease, which results in heart attacks, peripheral vascular disease that affects blood vessels of legs and feet and cerebrovascular disease that damage the blood vessels of brain. This increased scarring is due to the high blood sugar levels that ca lead to impairment of blood vessels and nerve of whole body [4].

The adverse effects of diabetes mellitus can be avoided with good glycemic control, regular screening for related issues and proper control of any existing complications. However if left untreated severe complications may arise in diabetic patients. These complications include oxidative stress, hyperlipidemia and enzymatic glycation of protein [5]. Fibric acid derivatives belong to a class of drugs known as fibrates, and they work by increasing the breakdown and elimination of triglycerides (TG) and cholesterol from the blood. Fiberates are an important class

*Corresponding Author:
majdabatool12@gmail.com (Majda Batool)

of lipid-lowering drugs. These reduces the risk of cardiovascular disease that is usually associated with high levels of blood lipids in body.

These drugs are most effective for the patients who have high levels of triglycerides (TG) that are the major cause for the development of cardiovascular disease. Gemfibrozil and fenofiberate are examples of fibric acid derivatives. Although these drugs effectively reduce the blood lipid levels but these are associated with many side effects such as liver disease, gastrointestinal problems and muscles fatigue [6].

Among patients with T2DM hyperlipidemia can increase the risk of cardiac arrest. It causes the deposition of fats (plaques) on the walls of blood vessels that results in atherosclerosis. Atherosclerosis can narrow the blood vessels and restrict blood supply to the heart, which can increase the risk of cardiac arrest. Moreover, patients with T2DM have more chances of developing cardiovascular disease, and hyperlipidemia can further promote the situation [7].

The diabetic hyperlipoproteinemia also known as atherogenic dyslipidemia is due to increased triglycerides TG, low density lipoproteins (LDL), and reduced levels of high density lipoproteins (HDL) cholesterol [8]. Compounds with five - membered rings having one or more heteroatoms are of great interest in drug design and medicinal chemistry due to their diverse pharmacological activities, high selectivity towards biological targets, and potential for the development of novel and effective drugs [9].

The 1,3,4-oxadiazole ring is a five-membered heterocyclic compound containing two nitrogen atoms and one oxygen atom. This ring system has gained attention from researchers as a potential replacement for carbonyl containing compounds e.g., carboxylic acids, esters, and amides in drug design. This substitution is known as a bioisostere, which means it has a similar shape and electronic properties to the original compound, allowing it to retain or improve upon the original compound's biological activity .In drug design, the oxadiazole ring is often used as an effective moiety of the pharmacophore. It can interact with the ligand, forming various chemical bonds that can influence the drug's affinity and selectivity for the target, as well as its pharmacokinetic properties. In some cases, the oxadiazole ring can act as a flat aromatic linker. This property makes it useful in drug design, where the linker can be tailored to optimize the molecule's properties, such as solubility, stability, and bio availability.

Overall, the 1,3,4-oxadiazole ring is a versatile and promising bioisostere that can improve the biological activity and pharmacokinetic properties of drug molecules. Its potential applications are vast and continue to be explored by researchers in the field of drug chemistry [10]. The compounds containing this characteristic oxadiazole moiety have been reported to exhibit diverse pharmachological activities such as antifungal [11], antibacterial [12], anti-mycobacterial [13], anticonvulsant [14], antidiabetic [15], anticancer, anti-inflammatory and analgesic [16]. So, it is an hour of need to have such a drug that have diversity and be able to spread its roots among all mechanisms and complications regarding diabetes mellitus.

The aim of our study is also centered to bring some drug with 1,3,4-oxadiazole moiety that is able to combat against frequently found complications. Previously we used ultrasonic method for the synthesis of 1,3,4-oxadiazole derivatives [17]. In continuation of our ongoing research, we have applied conventional and microwave-assisted synthetic strategies and achieved maximum yields of fibric acid 1,3,4-oxadiazole derivatives (3a-h) over shorter reaction times by microwave exposure. The titled compounds were further evaluated for their *in vivo* hypoglycemic potential.

2. Materials and Methods

2.1. Chemistry

Microwave-assisted synthesis was performed with a microwave apparatus Model EA-180M. Analytical grade chemicals were purchased from Sigma Aldrich and Alfa Aesar. Purity of synthesized compounds was checked by TLC G-25-UV254 plates by using ethylacetate : *n*-hexane (1:4) giving single spot. Griffin and George melting point apparatus were used for melting points by using open capillary tube method and reported as uncorrected. The synthesized scaffolds were recrystallized from 30% ethanol. 5-[2-(4-Chlorophenoxy) propan-2-yl]-1,3,4 - oxadiazol -2-thiol **(1)** [18] and aromatic *N*-substituted -2- bromoacetamides **(2a-h)** were synthesized by already reported protocol with slight modifications [19].

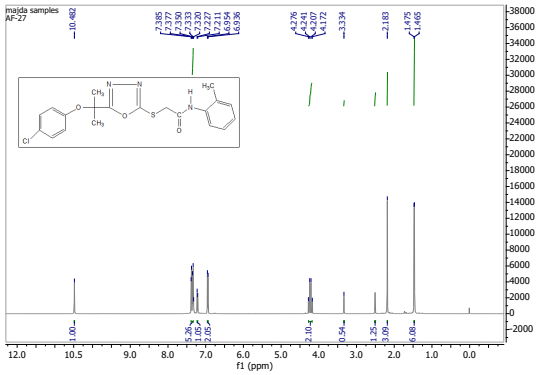

Figure 1. ^{1}H-NMR spectrum of compound **(3b)**

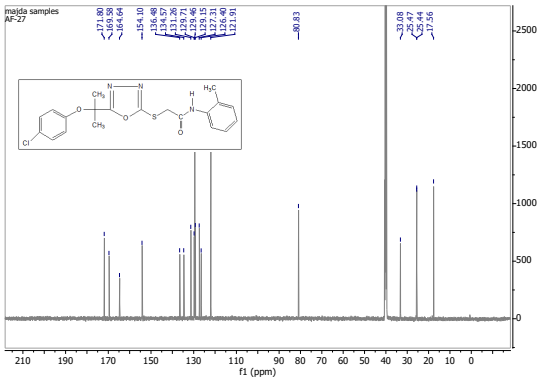

Figure 2. ^{13}C-NMR spectrum of compound **(3b)**

2.1.1. *Conventional method for synthesis of Fibric Acid 1,3,4-Oxadiazole Derivatives* ***(3a-h)***

To a solution of 5-[2 -(4-chloropropan-2-yl]-1,3,4 - oxadiazole - 2-thiol **(1)** (1 mmol) in DMF were added lithium hydride (2 mmol) as a catalyst and stirred at room temperature for half an hour. Then, *N*-substituted-2-bromoacetamide **(2a-h)** (1 mmol) was added as an electrophile, and the reaction mixture was further stirred at room temperature for 11-26 hours. The progress of reaction was monitored by TLC (using ethylacetate : n-hexane, 1:4) as mobile phase. On completion, the reaction mixture was poured over ice chilled water and the resulting precipitates were filtered, washed with distilled water, and dried to obtain the desired compounds **(3a-h)** in good yield (Table 3). The product **(3a-h)** was further recrystallized by using 30% ethanol.

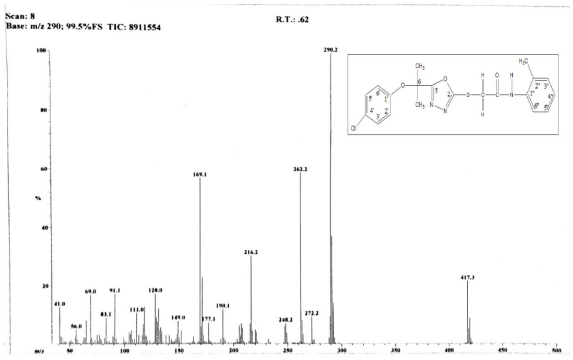

Figure 3. EI-MS of compound 3b

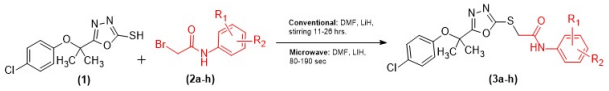

Figure 4. Scheme showing synthetic pathway for conventional / microwave assisted synthesis of acetamides (3a-h).

Table 1. Different substitutions in **(3 a-h)**

Codes	3a	3b	3c	3d	3e	3f	3g	3h
R^1	H	H	H	H	$2-CH_3$	$2-CH_3$	$2-CH_3$	$3-CH_3$
R^2	H	$2-CH_3$	$3-CH_3$	$4-CH_3$	$3-CH_3$	$4-CH_3$	$6-CH_3$	$4-CH_3$

2.1.2. *Microwave-assisted method for synthesis of Fibric Acid 1,3,4-Oxadiazole Derivatives* ***(3a-h)***

To a solution of 5-[2-(4-chloropropan-2-yl]-1,3,4 - oxadiazole - 2-thiol **(1)** (1 mmol) in DMF were added lithium hydride (2 mmol) as a catalyst and stirred at room temperature for half an hour. Then, *N*-substituted-2-bromoacetamide **(2a-h)** (1 mmol) was added as an electrophile and the reaction mixture was subjected to MW irradiations for 80-190 sec. The progress of reaction was monitored by TLC (using ethylacetate : n-hexane, 1:4) as the mobile phase. On completion, the reaction mixture was poured over ice chilled water and the resulting precipitates were filtered, washed with distilled water, and dried to obtain the desired compounds **(3a-h)** in good to excellent yield (Table 3) . The product **(3a-h)** was further recrystallized by using 30% ethanol.

2.2. *Biological Essay*

2.2.1. *Anti-hyperglycemic activity*

Experimental animals in this study were Sprague Dawley Albino rats weighing between 200-250 g. They were kept in an animal house at a controlled temperature of 25 ± 5°C and humidity of 50 ± 10%. The rats were given free access to pathogen-free feed and autoclaved tap water for 24 hours. All *in vivo* experiments were approved by the Institutional ethical committee (Approval No. D/017/Chem.) and followed international ethical guidelines to ensure the proper care and well-being of the rats in animal house.

2.2.2. *Oral glucose tolerance test in normal rats*

After 18 hours of starvation blood sugar level of each rat was measured by using a code-free glucometer. Rats with the blood sugar levels ranging between 80-100 mg/dL were grouped in sets of six. A single oral dose of the synthesized compounds (100 mg/kg body weight), was given to experimental group after emulsification in aqueous carboxymethyl cellulose (0.5%). Only aqueous CMC (0.5%) was given to control group. After exactly half an hour administration of vehicle/test sample, a glucose solution (2.0 g/kg body weight) was orally given to each rat. The blood sugar level of each rat was measured at 1, 3, and 5 hours intervals after the glucose administration [20].

3. Results and Discussion

3.1. *Chemistry*

Scheme of Microwave-assisted, a green synthetic technique that is environment friendly, economical, time saving affording excellent yield was adopted along with conventional method as shown in figure 4. The ultrasonic method of synthesizing the title compounds has been already reported [17] as affording fibric acid-oxadiazole derivatives **(3a-h)** in moderate to good (75-91%) yields. Purpose of the present study was to increase the yield and reduce the time for synthesis by applying the microwave-assisted approach to achieve the desired product as compared to conventional method. In conventional and microwave -assisted approach the scaffold 5-[2-(4-Chlorophenoxy) propan-2-yl] - 1,3,4-oxadiazole-2-thiol **(1)** was coupled with electrophiles, *N*-substituted-2-bromoacetamide **(2a-h)** to synthesize *N*-substituted 5 -[2-(4-chlorophenoxy) propan-2-yl]-1,3,4-oxadiazol-2-ylthio acetamides (**(3a-h)** Scheme shown in figure 4, Table 1). The ultrasonic technique yielded products of 75-91% in 60-90 minutes at room temperature as compared to conventional method that affords products of 41-69% in 11-26 hours at room temperature. The MW technique was much more efficient as the maximum yield of target compounds 82-96% in short period of time 80-190 seconds was obtained. The fibric acid derivative **(3h)** was obtained with maximum yield, while compound **(3a)** was achieved within least yield by all three synthetic protocols as mentioned in Table 3. The supposed

Table 2. Physical Parameters of *N*-substituted 5-[2-(4-chlorophenoxy)propan-2-yl]-1,3,4-oxadiazol-2-ylthioacetamides **(3a-h)**

Code	Appearance	Mol. formula	EIMS: m/z
3a	white fluffy amorphous flakes	$C_{19}H_{18}N_3O_3SCl$	403 [M^+, 2 %], 405 [M^{+2}, 0.8 %], 276 (100), 248 (5), 202 (13), 183 (20), 166 (30), 128 (26), 123 (64), 106 (22), 93 (13), 77 (11), 65 (13), 55 (8), 41 (9).
3b	Light yellow color powder	$C_{20}H_{20}N_3O_3SCl$	417 [M^+, 22 %], 419 [M^{+2}, 9 %], 290 (100), 272 (9), 262 (59), 248 (7), 216 (30), 190 (12), 177 (7), 169 (57), 149 (8), 128 (17), 111(11), 91 (17), 83 (9), 69 (17), 56 (5), 41 (13).
3c	Lemon yellow color powder	$C_{20}H_{20}N_3O_3SCl$	417 [M^+, 12 %], 419 [M^{+2}, 4 %], 290 (100), 272 (4), 262 (18), 248 (3), 216 (25), 183 (35), 169 (24), 148 (12), 138 (35), 138 (25), 123 (71), 107 (16), 91 (17), 69 (10), 41 (7).
3d	Dirty white color powder	$C_{20}H_{20}N_3O_3SCl$	417 [M^+, 5 %], 419 [M^{+2}, 2 %], 290 (100), 262 (5), 216 (7), 183 (24), 148 (10), 138 (22), 123 (55), 91 (8), 55 (5), 41 (5).
3e	Creamy white color powder	$C_{21}H_{22}N_3O_3SCl$	431 [M^+, 38 %], 433 [M^{+2}, 14 %], 304 (100), 286 (12), 276 (88), 261 (8), 230 (15), 219 (13), 204 (32), 191 (11), 169 (72), 152 (8), 145 (17), 128 (15), 105 (12), 77 (7), 69 (16), 56 (6), 41 (14).
3f	Golden yellow color powder	$C_{21}H_{22}N_3O_3SCl$	431 [M^+, 17 %], 433 [M^{+2}, 7 %], 304 (100), 286 (7), 276 (13), 262 (2), 230 (24), 204 (4), 194 (32), 183 (41), 162 (21), 152 (37), 128 (32), 123 (81), 83 (11), 55 (7), 41 (10).
3h	Off-white color powder	$C_{21}H_{22}N_3O_3SCl$	431 [M^+, 11 %], 433 [M^{+2}, 5 %], 304 (100), 276 (9), 230 (12), 194 (23), 183 (42), 169 (14), 162 (20), 152 (37), 128 (22), 123 (84), 109 (10), 91 (9), 77 (10), 55 (6), 41 (9).

Table 3. Comparison of conventional, Ultrasonic and microwave-assisted methods

Compound	Reaction Yield (%)			Reaction Time			Melting Point (°C)	
	Conventional	Ultrasonic	Microwave	Conventional (hour)	Ultrasonic (minute)	Microwave (second)	Found	Reported [17]
3a	41	75	82	11	60	80	84	84-86
3b	62	87	93	23	80	155	141	140-142
3c	46	78	85	19	75	140	71	71-72
3d	55	84	89	12	60	84	68	68-70
3e	60	86	91	26	90	190	186	186-188
3f	52	81	88	24	80	160	79	78-80
3g	65	89	94	12	60	86	98	98-100
3h	69	91	96	17	70	124	80	80-82

structures of synthesized compounds **(3a-h)** were confirmed by spectral data [17].

The synthesized compound **(3b)** was obtained as light yellow color powder having yield 87% and m.p. 140-142°C. Molecular formula $C_{20}H_{20}N_2O_3SCl$ was confirmed by EI-MS showing molecular ion peak at 290 (Figure 3). In FTIR spectrum peaks for N−Hstretching appeared at 3339, for C−H stretching of aromatic ring 2981, C=O amide stretching 1667, C=C aromatic ring stretching at 1484. ^{1}H-NMR results show peak at 10.48 as a singlet for NH. A multiplet at 7.38-7.32 represents two aromatic protons of fibric acid moiety (H-3´, H-5´) and three aromatic protons of acetamide group (H-4´´, H-5´´ & H-6´´). Appearance of four doublets at 7.22, 6.94, 4.26 and4.19 confirm proton H-3´, H-2´´ & H-6´´, Ha and Hb respectively. Three singlets at 2.18, 1.47 and 1.48 represents three protons of aromatic CH_3 and six protons of fibric acid aliphatic region (Fig.1). These cumulative spectral evidences determine the structure as 2-5-[2-(4-Chlorophenoxy)propan-2-yl]-1,3,4-oxadiazol-2-ylthio-N-(2-methylphenyl)acetamide. All spectral results from FT-IR, ^{1}H-NMR, ^{13}C-NMR and EI-MS thoroughly confirm the structure of remaining fibric acid derivatives **(3a-h)**.

Table 4. OGTT in normal rats

Sr. No.	Compounds	Glucose level mg/dL			
		Fasting	1 hr	3 hr	5 hr
1	1	91	109	85	84
2	3a	74	102	84	72
3	3b	69	114	85	83
4	3c	80	119	96	89
5	3d	79	122	104	104
6	3e	82	128	104	103
7	3f	88	121	109	101
8	3g	75	89	81	78
9	3h	81	113	90	74
10	Control	99	100	79	75
11	Glibenclamide	93	76	49	42

3.2. Pharmacology

From the Table 4, it can be observed that compounds **(3a-h)** have varying effects on glucose levels as compared to the control group and glibenclamide. Compound **(3c)** has a slightly higher fasting glucose level than the control group, but it shows a reduction in glucose levels at 1 hour, 3 hours, and 5 hours after treatment. The glucose-lowering effect of **(3c)** is comparable to that of glibenclamide. However, compounds **(3d)**, **(3e)**, and **(3f)** show a reduction in glucose levels at 1 hour after treatment but do not maintain this effect at 3 hours and 5 hours after treatment. Compound **(3g)** shows a reduction in glucose levels at all time points after treatment but to a lesser extent than 3c and glibenclamide. Compound **(3h)** shows a reduction in glucose levels at 1 hour and 3 hours after treatment but not at 5 hours after treatment.

Overall, the above results suggest that compound **(3c)** has potential as an anti-diabetic agent as it shows a sustained glucose-lowering effect comparable to glibenclamide. However, further more studies are needed to assess the safety and efficacy of this compound in the treatment of diabetes.

4. Conclusion

Our results revealed that the Synthesis of titled compounds, **(3a-h)**, by microwave- assisted method resulted into high yield within 80-190 seconds with maximum yield of 82-96% as compared to ultrasonic and conventional techniques that afforded products of 75-91% in 60-90 minutes and 41-69% in 11-26 hours respectively (Table 3). The spectroscopic data well supported the supposed structures of synthesized compounds. The compound **(3c)** showed good anti-hyperglycemic activity in normal hyperglycemic rats. This may be due to methyl substitution at ortho position of phenyl ring of amide. On the basis of above results, it was concluded that the compounds **(3a-h)** may be used as drug candidates suitable for hypoglycemia and other related diseases.

References

[1] A. Bukhari, H. Nadeem, M. Imran, S. A. Muhammad, Novel oxadiazole derivatives as potent inhibitors of α-amylase and α-glucosidase enzymes: Synthesis, in vitro evaluation, and molecular docking studies, Iranian Journal of Basic Medical Sciences 24 (12) (2021) 1632.

[2] E. Chiefari, B. Arcidiacono, D. Foti, A. Brunetti, Gestational diabetes mellitus: an updated overview, Journal of endocrinological investigation 40 (2017) 899–909.

[3] A. Anık, G. Çatlı, A. Abacı, E. Böber, Maturity-onset diabetes of the young (mody): an update, Journal of pediatric endocrinology and metabolism 28 (3-4) (2015) 251–263.

[4] K. G. M. M. Alberti, P. Z. Zimmet, Definition, diagnosis and classification of diabetes mellitus and its complications. part 1: diagnosis and classification of diabetes mellitus. provisional report of a who consultation, Diabetic medicine 15 (7) (1998) 539–553.

[5] H. Al-Hourani, M. Atoum, et al., Body composition, nutrient intake and physical activity patterns in young women during ramadan, Singapore medical journal 48 (10) (2007) 906.

[6] G. A. Idrees, O. M. Aly, G. E.-D. A. Abuo-Rahma, M. Radwan, Design, synthesis and hypolipidemic activity of novel 2-(naphthalen-2-yloxy) propionic acid derivatives as desmethyl fibrate analogs, European journal of medicinal chemistry 44 (10) (2009) 3973–3980.

[7] L. Zhu, A. Hayen, K. J. Bell, Legacy effect of fibrate add-on therapy in diabetic patients with dyslipidemia: a secondary analysis of the accordion study, Cardiovascular diabetology 19 (1) (2020) 1–9.

[8] A. D. Mooradian, Dyslipidemia in type 2 diabetes mellitus, Nature Reviews Endocrinology 5 (3) (2009) 150–159.

[9] K. Peregrym, Ł. Szczukowski, B. Wiatrak, K. Potyrak, Ż. Czyżnikowska, P. Świątek, In vitro and in silico evaluation of new 1, 3, 4-oxadiazole derivatives of pyrrolo [3, 4-d] pyridazinone as promising cyclooxygenase inhibitors, International Journal of Molecular Sciences 22 (17) (2021) 9130.

[10] J. Bostrom, A. Hogner, A. Llinas, E. Wellner, A. T. Plowright, Oxadiazoles in medicinal chemistry, Journal of medicinal chemistry 55 (5) (2012) 1817–1830.

[11] F. Liu, X.-Q. Luo, B.-A. Song, P. S. Bhadury, S. Yang, L.-H. Jin, W. Xue, D.-Y. Hu, Synthesis and antifungal activity of novel sulfoxide derivatives containing trimethoxyphenyl substituted 1, 3, 4-thiadiazole and 1, 3, 4-oxadiazole moiety, Bioorganic & medicinal chemistry 16 (7) (2008) 3632–3640.

[12] B. S. Holla, R. Gonsalves, S. Shenoy, Synthesis and antibacterial studies of a new series of 1, 2-bis (1, 3, 4-oxadiazol-2-yl) ethanes and 1, 2-bis (4-amino-1, 2, 4-triazol-3-yl) ethanes, European journal of medicinal chemistry 35 (2) (2000) 267–271.

[13] F. Macaev, G. Rusu, S. Pogrebnoi, A. Gudima, E. Stingaci, L. Vlad, N. Shvets, F. Kandemirli, A. Dimoglo, R. Reynolds, Synthesis of novel 5-aryl-2-thio-1, 3, 4-oxadiazoles and the study of their structure–antimycobacterial activities, Bioorganic & medicinal chemistry 13 (16) (2005) 4842–4850.

[14] A. Zarghi, S. A. Tabatabai, M. Faizi, A. Ahadian, P. Navabi, V. Zanganeh, A. Shafiee, Synthesis and anticonvulsant activity of new 2-substituted-5-(2-benzyloxyphenyl)-1, 3, 4-oxadiazoles, Bioorganic & Medicinal Chemistry Letters 15 (7) (2005) 1863–1865.

[15] K. G. Liu, J. S. Smith, A. H. Ayscue, B. R. Henke, M. H. Lambert, L. M. Leesnitzer, K. D. Plunket, T. M. Willson, D. D. Sternbach, Identification of a series of oxadiazole-substituted α-isopropoxy phenylpropanoic acids with activity on pparα, pparγ, and pparδ, Bioorganic & medicinal chemistry letters 11 (17) (2001) 2385–2388.

[16] E. Palaska, G. Şahin, P. Kelicen, N. T. Durlu, G. Altinok, Synthesis and anti-inflammatory activity of 1-acylthiosemicarbazides, 1, 3, 4-oxadiazoles, 1, 3, 4-thiadiazoles and 1, 2, 4-triazole-3-thiones, Il Farmaco 57 (2) (2002) 101–107.

[17] M. Batool, A. Tajammal, F. Farhat, F. Verpoort, Z. A. Khattak, M. Shahid, H. A. Ahmad, M. A. Munawar, M. Zia-ur Rehman, M. Asim Raza Basra, Molecular docking, computational, and antithrombotic studies of novel 1, 3, 4-oxadiazole derivatives, International Journal of Molecular Sciences 19 (11) (2018) 3606.

[18] T. Ramlingam, P. Sattur, Synthesis and pharmacology of 2, 5-disubstituted 1, 3, 4-oxadiazoles, J. Ind. Chem. Soc 58 (1981) 269.

[19] P. R. Kagthara, N. S. Shah, R. K. Doshi, H. Parekh, Synthesis of 2, 5-disubstituted 1, 3, 4-oxadiazoles as biologically active heterocycles.

[20] A. Tajammal, M. Batool, A. Ramzan, M. M. Samra, I. Mahnoor, F. Verpoort, A. Irfan, A. G. Al-Sehemi, M. A. Munawar, M. A. R. Basra, Synthesis, antihyperglycemic activity and computational studies of antioxidant chalcones and flavanones derived from 2, 5 dihydroxyacetophenone, Journal of Molecular Structure 1148 (2017) 512–520.

Available online at www.rpnsci.com

Research Prospects in Natural Sciences, Vol. 1, Issue 1, (2023) 7–13

Research Article

Extraction of sustainable dye from *Syzygium cumini* for various fibers

Lubna Liaquat[a], Phool Shahzadi[a,*], Alim-un-Nisa[a], Zeeshan Ali[a], Azra Yaqoob[a], Razia Kalsoom[b], Abdur Rehman[c]

[a]*PCSIR Laboratories Complex, Lahore 54600, Pakistan.*
[b]*PCSIR Laboratories Complex, Islamabad, Pakistan.*
[c]*Institute of Metallurgy and Materials Engineering, University of the Punjab, Lahore 54000, Pakistan.*

Abstract

This study examines the extraction and application of *Syzygium cumini* bark dye on textile fibers using different mordant combinations. Mordants such as $FeSO_4$, oxalic acid, $SnCl_2$, and alum were applied in 1:1 and 2:1 ratios to develop various shades. The dye showed good performance on jute fibers, with dyed samples exhibiting good to excellent color fastness properties.

Keywords:
Jute, Dyeing, Sustainable Dye, Jambolan (Jamun) .

1. Introduction

Traditionally, people have dyed textiles using locally available natural materials that produce bright and durable colors, such as Jamun bark [1]. Natural dyes were relatively inexpensive, offered a wide range of shades, and improved the overall quality of dyed materials [2]. Natural dyeing practices are as old as textile coloration itself, although historically only a limited proportion of textiles were colored using plant-based dyes. In recent years, growing consumer awareness of the environmental and ecological concerns associated with synthetic dyes has renewed interest in natural dyes [3–6]. *Syzygium cumini* Linn, an evergreen tree belonging to the family Myrtaceae, is one such potential source of natural dye.

The jambolan plant, commonly known as Jamun or black plum (*Syzygium cumini* Linn), is a well-known species belonging to the family Myrtaceae [2]. It is a fast-growing evergreen tree that can reach heights of up to 25m, characterized by a grayish-white young stem and a coarse, darkened lower bark [7–10]. The stem bark is considered one of the most potent parts of the plant due to its high tannin content, particularly gallic acid, which contributes to its astringent properties. The deep purple coloration of the fruit is attributed to the presence of cyanidin diglycosides [11]. Ripe fruits of *Syzygium cumini* are widely used in the preparation of beverages, squashes, jellies, wines, and preservatives [12]. In addition to its dietary applications, the seeds are traditionally used to manage various ailments, notably diabetes mellitus [13]. Different parts of the Jamun plant have been reported to exhibit antioxidant, anti-inflammatory, neuropsychopharmacological, antibacterial, antifungal, anti-ulcerogenic, hypoglycemic, and radioprotective activities, attributed to the presence of tannins, flavonoids, essential oils, and organic acids [14, 15]. An astringent decoction prepared from Jamun bark is also traditionally used for gargling purposes.

The herbal dyeing process involves three major steps [16, 17]. The first step is the extraction of the colorant from plant parts such as stems or bark. This is followed by the formation of a bond between the extracted coloring matter and the textile fiber, a process facilitated by the use of a mordant. The final step is the actual dyeing of the fiber. Mordanting enables effective fixation of the dye on the fiber, leading to the development of new shades with improved color fastness and reproducible color yield. As most natural dyes are non-substantive in nature, they require the use of mordants such as stannous chloride ($SnCl_2$), potash alum, ferrous sulfate ($FeSO_4$), and oxalic acid for effective application on textiles. Linn. can reach heights of 20?25 m with a girth of 2?3 m and may live up to 100 years

*Corresponding Author:
psk717@gmail.com (Phool Shahzadi)

in suitable locations. Its medicinal properties are primarily attributed to compounds such as maleic acid, oxalic acid, gallic acid, and tannins [18–21]. While the entire plant is used in traditional medicine, the leaves and stem bark are considered the most potent parts, with gallic acid in the bark largely responsible for its astringent effects. The purple coloration of the fruit is due to cyanidin diglycosides [22–24]. Various studies have reported that tannins, flavonoids, essential oils, and organic acids in Jamun exhibit diverse pharmacological activities, including gastroprotection, anti-ulcerogenic, antibacterial, anti-infective, anti-inflammatory, hypoglycemic, antioxidant, and radioprotective effects [25–27]. Additionally, an astringent decoction prepared from Jamun bark is traditionally used as a gargle [28]

2. Materials and Methods

2.1. Preparation of raw materials

The raw material of Jambolan bark are cut from the trunk of Jambolan tree and they were cleaned with water by brushing to remove the impurities and allowed to soak in warm water for 12 hours then heated and boiled for 1-2 hour. After than slowly heated and boiled for 2-3 hours at 90°C reduce the extraction time silvaaetal L007. One hundred gram of Jambolan bark powder are placed in a round bottom flask with 500 ml of water are added into it. The flask is heated in water bath at 60°C for one hour. The above processes repeated 3 times at 60°C. The extracted dye solution put into the petridish for evaporation of water. After extracting the dye from dye solution is dried in the oven at 60°C. This dyestuff is extracted as powder form after evaporation.

Post mordanting technique are applied for dye the Jute. It is technique which applied after dyeing the fiber a mordant can give color. The dyed material is treated with a mordant which are used the fix a dye with fiber ad give the color. They also improve the take up quality of fiber, color and light fastness.

2.2. Chemicals

Detergent ECE (without optical brightener) sodium per borate, 1-histidine monochloride monohydrate, sodium dihydrogen orthophosphate, distilled water, sodium carbonate, sodium hydroxide, acetic acid, sulphuric acid, and perchloroethylene solvent. All the chemicals and solvents used were of AR grade.

2.3. Collection of Bark and Extraction of Color

Jamun bark was purchased from Murree market and thoroughly washed with water and dried. It was ground into powder and sieved through 22 mesh size strainer. 500 g bark powder was soaked in 5 L water over night, boiled for 2 to 3 h and then subjected to stirring for 3 to 4 h at simmering temperature. A dark brown colored due solution obtained which was filtered and kept for dyeing and other tests.

2.4. Color Fastness to washing

The dyed sample Jute was shaked with detergent solution for 30 minutes report that rinsing procedure once more with a new rinsing float. Dried the sample and extent of fading examined the wash fastness rating was assessed using grey scale. Instruments D400IR dyeing machine (SDL Atlas Englang); Launderometer (Roaches), Perspirometer kit (SDL Atlas England); oven Ci 3000 + Xenon: weatherometer (Atlas England); water bath; grey scales for staining (ISO 105 A03); grey scale for change in shade (ISO A02); crockmeter 9SDL Atlas England); multifiber (DW).

2.5. Dyeing with Jamun bark

Fabric of cotton, Jute and silk 20 g each were dyed with same depth of jamun bark dye, bark dye extract in the D400 IR dyeing machine (SDL Atlas England) at 100°C for 1 h with speed of circulation 1.5 rpm.

2.6. Fastness determination

Wash fastness test of all the three dyed fabrics was determined according to ISO 105 C06 method. Light fastness was examined according to ISO 105 standard method procedure B02. Rubbing fastness (dry and wet) test was carried out according to ISO 105x12 standard test procedure. Color fastness tests to dry cleaning, water, sea water, and perspiration (acidic and basic) were carried out according to ISO 105:D01,E01,E02 and E04 methods, respectively. Color fastness to spotting of acids and alkalies test were performed according to ISO E05 and E06 methods, respectively (BS 1006:1990).

2.7. Washing Fastness

Washing fastness was determined by preparing the soap solution containing 4 g detergent and 1 g sodium perborate per liter of distilled water. pH was adjusted to 10.5+0.1 by addition of approx. 1 g of sodium carbonate. Jute, cotton and silk fabric pieces of size 10x4 cm were attached to multifiber DW of the same measurements by sewing along with one of the shorter sides. Three composite specimens were put into glasses of launderometer (Roaches) for 30 min at 60°C having liquor ratio 50:1.Launderometer or Washtec consists of a water bath containing a rotatable shaft which supports radially, stainless steel container (75+5 mm diameter x 125+10 mm height) of capacity 550+50ml, the bottom of container being 45+10 from the center of shaft. The shaft/container assembly is rotated at a frequency of 40+2/min. After 30 min, samples were removed from the Washtec. Stitches were removed and the specimens were dried at temperature not more than 60°C. The change in stain and shade was assessed with the help of grey scale.

2.8. Color Fastness to Perspiration

Test were carried out by dipping the fabrics into 1-histidine monohydrochloride monohydrate solution according to ISO 105 E04 method. Specimens of Jute, cotton and silk of 4 cm x 10 cm measurement were attached to pieces of multifibre of the same measurement by sewing along with one of shorter sides and dipped separately into alkaline and acidic solutions for 30

min having liquor ratio 50:1. Then the Jute, cotton and silk specimens were placed in the perspirometer kits and the desired pressure was applied. Perspirometer kits are test devices each consisting of a frame of stainless steel into which a weight piece of ass 5 kg and base of 60 mm x115 mm is closely fitted so that a pressure of 12.5 kpa can be applied on test specimens measuring 40 mm x 100 mm, placed between glass or acrylic resin plates measuring 60 mm x 115 mm x 1.5mm. The test device is constructed in such a way that a pressure of 12.5 kpa remains unchanged. The perspirometer kits (acidic and basic) for tests of the three fabrics were placed in the vacuum oven for 4 h and then the kits were removed from the oven and the stitches were opened except on one shorter side. Specimens were dried at 60°C by hanging in air. Change in color of each specimen and staining of the adjacent fabric (DW) were assessed with grey scale.

2.9. Rubbing Fastness

Dry rubbing on Jute was carried out with the help of crockmeter under a pressure of 9 N in to and fro movements on standard rubbing cloth. The sample cotton of 5 cm x 14 cm measurement was taken. Both warp and weft readings were noted. Same procedure was adopted for jute and silk and values were taken with the help of grey scale.

2.10. Wet rubbing

Wet rubbing on Jute fabric was done under the same conditions of crockmeter as in the dry rubbing except the standard rubbing soaked into 100% deionized water. Same procedure was repeated with cotton and silk fabrics and the change in color and in stain was assessed with the help of grey scale.

2.11. Light Fastness

Light fastness was carried out according to ISO 105 standard procedure B02; in weatherometer by Atlas. Xenon arc lamp was used which is an artificial light source representative of natural day light D65. Fabrics of measurement 7 cm x 12 cm of cotton Jute and silk were exposed to Jamun bark dye and color fastness. Xenon arc lamp for 24 h, at standard testing conditions using blue wool as standard reference fabric. The above three treated fabrics were compared with grey scale for evaluation.

2.12. Color Fastness to Dry Cleaning

Undyed Jute twill bags of 10cm x 10 cm measurement were stitched around three sides and Jute. Jute silk pieces of 4 cm x 10 cm measurement were placed into separate bags along with 12 non-corrodable steel disks and the fourth side of the bag was sewed. Then the bags were placed in separate containers of Washtec containing 200 ml of perchloroethylene solvent and agitated for 30 min at 30+2°C. Afterwards the bags were removed from the container. The samples were squeeze to remove surplus solvent and dried in the air by hanging them at a temperature of 60+5 °C. Assessment of change in color of samples and change in color of solvent was carried out with the help of grey scale.

2.13. Color Fastness to Water

Color fastness to water was evaluated in the same manner as for the color fastness to perspiration. ISO-105 E01 and E02 methods was used for water and sea water, repectively. In case of water, fabrics were dipped in deionized water, while for color fastness to sea water, fabrics along with multifibers were dipped in NaCl solution (30 g/l) for 30 min.

For both water and sea water the above three treated composite fabrics were put in perspirometer kit. These kits were placed in the oven for 4 h at 37+°C. Then the specimens were dried at temperature not more than the specimens were dried at temperature not more than 60°C. Change in shade and in stain were noted with the help of grey scale.

2.14. Color Fastness to Dry Heat

Dry hot pressing was done according to ISO 105 XII. Specimens of Jute, cotton and silk were pressed at temp. 110+2 °C with hand iron and change in color was assessed with grey scale .

2.15. Color Fastness to Spotting Acids and Alkali

Scope of acetic acid 300 g/l, sulphuric acid 50 g/l, tartaric acid 100 g/l and Na_2CO_3, 100 g/l of water were put on the specimens and change in shade was assessed with ISO-105 A02 grey scale.

3. Results and Discussion

3.1. Antioxidant Activity of Sweet Lime Peel

The dyed textile was immersing in separate vessel in the artificial perspiration solution placed the specimen between two glass plates in the apparatus and loaded it with a weight of 4.5 Kg, placed it in the oven at 37+2°C for three hours at 37+2°C for houses in color of scale (AAtCC-1995). At the end of this period sample was removed and the test piece was separate from the two pieces of the untreated fabric and dried in air at a temperature not exceeding 60°C.

The dyed sample of wet/dry Jute fabric were placed over the end of finger of testing device and rubbed. Over to end of the finger of the testing device and rubbed it to and form in a straight line. The pieces were dried at room temperature. The degree of fabric was evaluated with to help of grey scale and the numerical rating were assigned.

3.2. Change in staining

When the washing fastness characteristics of cotton, jute cotton, and silk were tested, it was found that the staining performance of jute and silk textiles was excellent (5) on a diacetate band of multi-fiber DW for jute fabric. Staining was good for jute fabrics (4-5) rating and (4) for cotton fabric for multifiber cotton band. Cotton fabric produced outcomes for the nylon band of multi-fiber that were satisfactory (3-4) and good (4-5) for jute and silk. All fabrics for polyester band received the same grade of 4. All three fabrics for the polyacrylic and cotton band received an outstanding (5) stain grade (Table 1).

Table 1: Fastness grades of Jute dyed with Jambolan colorant with at optimum dyeing condition using $SnCl_2$: Oxalic acid

Mordanting	Mordanting portion or ratio combination	Light Fastness	Wash Fastness			Rub Fastness				Fastness Perspiration		
						Dry			Wet			
			CC	CS	CJ	CC	CS	CJ	CC	CS	CC	CJ
Post mordanting by $SnCl_2$ + oxalic acid	1:1	4 - 4.5	5	5	5	5	5	5	4.5	5	5	5
	1:2	4 - 4.5	4	5	5	5	5	5	4.5	5	5	5
	1:3	4 - 4.5	4.5	5	5	5	5	5	4.5	5	5	5

C = Cotton, S = Silk, J = Jute

Table 2: Fastness grades of Jute dyed with Jambolan Colorant at optimum dyeing condition using $SnCl_2$: Ferrous sulfate

Mordanting	Mordanting portion	Light Fastness	Wash Fastness			Rub Fastness				Fastness Perspiration		
						Dry			Wet			
			CC	CS	CJ	CC	CS	CJ	CC	CS	CC	CJ
Post mordanting by $SnCl_2$ + $FeSO_4$	1:1	4 - 4.5	5	5	5	5	5	5	4.5	5	5	5
	1:2	4 - 4.5	4	5	5	5	5	5	4.5	5	5	5
	1:3	4 - 4.5	4.5	5	5	5	5	5	4.5	5	5	5

C = Cotton, S = Silk, J = Jute

Table 3: Fastness grades of Jute dyed with Jambolan Colorant at optimum dyeing condition using $SnCl_2$: Potash Alum

Mordanting	Mordanting portion	Light Fastness	Wash Fastness			Rub Fastness				Fastness Perspiration		
						Dry			Wet			
			CC	CS	CJ	CC	CS	CJ	CC	CS	CC	CJ
Post mordanting by $SnCl_2$ + Potash	1:1	4.5	5	5	5	5	5	5	4.5	5	5	5
	1:2	4.5	4	5	5	5	5	5	4.5	5	5	5
	1:3	4.5	4.5	5	5	5	5	5	4.5	5	5	5

C = Cotton, S = Silk, J = Jute

Table 4: Rubbing fastness, light fastness and color fastness to dry cleaning

Fabric	Rubbing fastness		Light fastness		color fastness to dry cleaning		
	Dry wrap	Rubbing wet	Wet wrap	Rubbing wet	Change in shade of fabric	Change in shade of fabric	Change in shade of solvent
Jute	4 - 5	4 - 5	3 - 4	4	4	5	5
Cotton	4 - 5	4 - 5	3 - 4	3 - 4	4 - 5	5	5
Silk	5	5	4 - 5	4 - 5	4	5	5

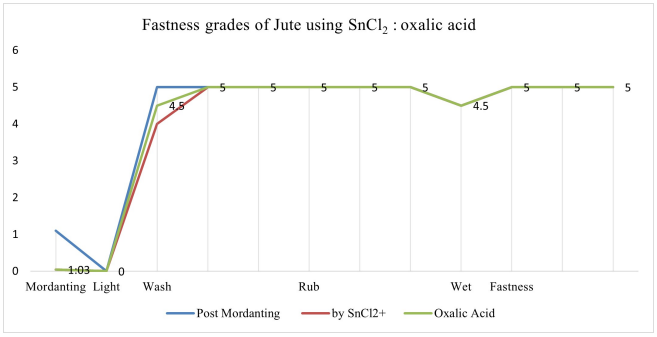

Figure 1: Fastness grades of Jute using $SnCl_2$: oxalic acid

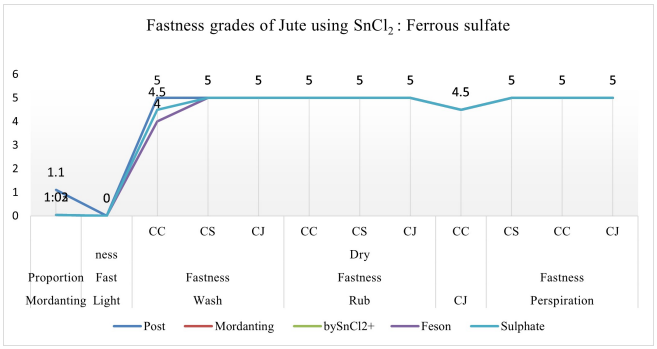

Figure 2: Fastness grades of jute using $SnCl_2$: Ferrous sulfate

3.3. *Change in shade*

Jute received a satisfactory (3-4) assessment for the results of change in color. Jute receives a grade of 4, while silk has a bad (2-3) rating compared to the other two textiles. Table 1 shows the results for shade changes for jute, cotton, and silk dyed with walnut bark extract.

3.3.1. *Jute fabric*

The results of acidic and basic sweat on a jute cloth on diacetate band were favorable (4-5). Acidic and basic sweat on a jute and nylon band produced staining results of 4. Both basic and acidic sweat produced great results (5) for the polyester band. Excellent (5) for acidic perspiration and good (4-5) for basic perspiration were discovered for polyacrylic band. Results for both perspirations for wool band were favorable (4-5). For acidic sweat, the change in shade was 4, however for basic perspiration on jute cloth, it was good (4-5). Excellent (5) rating was given for the multifiber diacetate band by acidic and basic sweat. For Jute bands, the stain change for both acidic and basic sweat was favorable (4-5). The staining for the nylon band was the same, or (4). Both sweat and polyester and polyacrylic band staining were excellent (5). Wool band also produced good (4-5) and excellent (5) staining for basic and acidic sweat, as well as good (4-5) and outstanding (5) shade changes for both types of perspiration.

3.3.2. *Silk fabric*

The diacetate band demonstrated outstanding (5) rating for basic perspiration and good (4-5) rating for acidic perspiration for silk fabric treated with walnut dye. For multifiber Jute bands, the stain change was good (4-5) for basic sweat and outstanding (5) for acidic sweat. For both acidic and basic sweat, polyester band staining received an excellent (5) rating. Excellent (5) for basic perspiration and good (4-5) for acidic perspiration for silk fabric were the results for polyacrylic band. Basic and acidic perspiration from nylon bands produced satisfactory (4-5) results on silk. Silk fabric received a favorable (4-5) assessment from the wool band for both acidic and basic sweating. The rating for basic perspiration was outstanding (five), while the rating for acidic perspiration was good (four to five).

3.4. *Light fastness*

Results of the light fastness test for jute, wool, and silk dyed with extract of walnut bark are displayed in Table 2. While cotton received a decent grade (4-5), jute and silk received a rating of 4. Dry cleaning. Results of color change for jute, cotton, and silk materials were outstanding (5). Excellent solvent color change was also seen (5) for all three textiles.

3.5. *Rubbing fastness*

3.5.1. *Dry rubbing fastness*

While silk fabric displayed outstanding rating (5) for dry rubbing fastness along warp and weft, jute and cotton both provided good ratings (4-5) for this property.

3.5.2. *Wet Rubbing fastness*

Wet rubbing along the warp for jute fabric was 3-4, which was satisfactory and acceptable. There were four weft wet rubbings. Wet rubbing fastness along warp and weft for woolen fabrics was 3-4, which is also acceptable. Silk fabric received a good (4-5) wet rubbing fastness grade along the warp and weft. The outcome is displayed in Table 2.

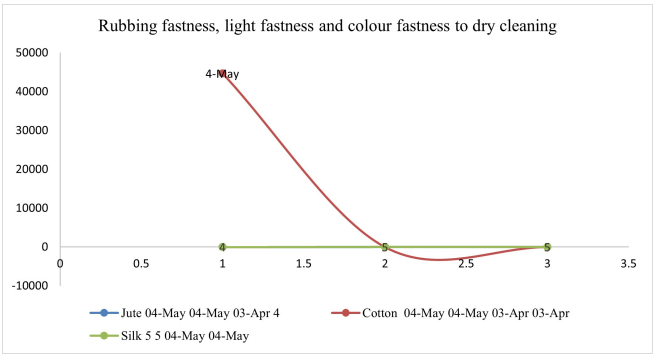

Figure 3: Rubbing fastness, light fastness and color fastness to dry cleaning

3.6. *color fastness to water*

3.6.1. *Change in stain*

Diacetate band received a good (4-5) grade for jute fabric. The assessment of stain change for fabrics made of wool and silk was outstanding (5). All three fabrics for the multifiber DW's jute band displayed the same grade, a respectable

4-5. For staining on nylon band, jute and silk had ratings of 4, whereas wool received ratings of (4-5). Results for the polyester band were excellent (5) across all three fabrics. Jute and silk received a reasonable grade (4-5) on the polyacrylic band, whereas wool received an exceptional rating (5). For Jute staining, the wool band of multifiber gave a rating of 4, 4-5 for Jute, and a rating of 5 for silk fabric (Table 3).

3.6.2. Change in shade

For all three materials, the rating for color fastness to water change was good (4-5). In Table 3, results are displayed.

3.7. Color fastness to sea water

Table 3 includes the results of color fastness to sea water. Staining. Jute fabric demonstrated a staining grade of 4, wool demonstrated an exceptional rating of 5, and silk had a decent (4-5) rating. Excellent (5) grade for the staining of jute, wool, and silk with walnut bark dye was given to the multifiber jute band. Wool and silk received fair (4-5) results from nylon band, whereas jute fabric received an exceptional (5) rating. For Jute fabric, the polyester band gave a good staining grade (4-5) and an exceptional rating (5) for both wool and silk. Jute, wool, and silk received stain ratings of 5, 4-5, and 4 from the wool band of multifiber (DW) (Table 3).

3.8. Color fastening speed to water

Change the color of. Diacetate band received a fantastic (4-5) grade for jute texture. The modify in recolor rating for woolen and silk texture was amazing (5). All three textures for the multifiber DW's jute band looked to be rated the same, at 4-5, which was excellent. Jute and silk provided ratings of 4 for recoloring in nylon band, whereas woolen provided ratings of (4-5). For all three textures, polyester band developments were excellent (5). Excellent grade (4-5) for Jute and Silk and fantastic rating (5) for Fleece were given to the polyacrylic band. For Jute's ability to change color, the fleece band of multifiber awarded it a rating of 4, 4-5, and 5 (Table 3). Alter in shade For all three textures, the rating for how quickly colors changed in the presence of water was excellent (4-5). The results are shown in Table 3.

3.9. Color quickness to ocean water

Table 3 also includes result of color reactivity to ocean water.

3.10. Recoloring

Jute texture looked to be rated at 4, fleece at rated at 5, and silk at rated at 4-5 for recoloring on the diacetate band. Jute band of multi-fiber looked fantastic, earning a grade of five (5). The nylon band gave fleece, silk, and jute a great (4-5) and great (5) rating, respectively. fantastic rating (5) for both fleece advertisement silk and fantastic (4-5) rating for Jute texture were given by the polyester band, along with great rating (4-5) for Jute recoloring. Jute, fleece, and silk, individually, received 5, 4-5, and 4 recolor ratings from the fleece band of multifiber (DW) (Table 3).

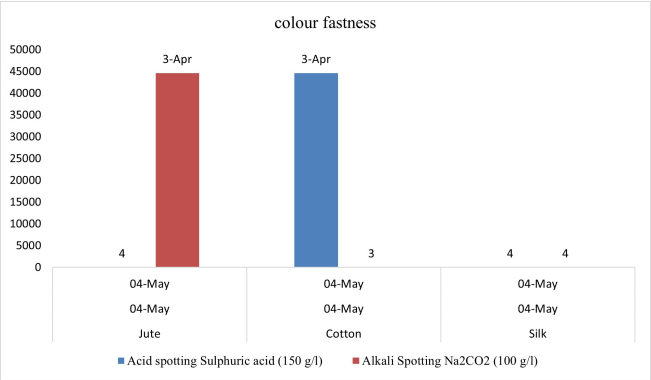

Figure 4: Results of color fastness

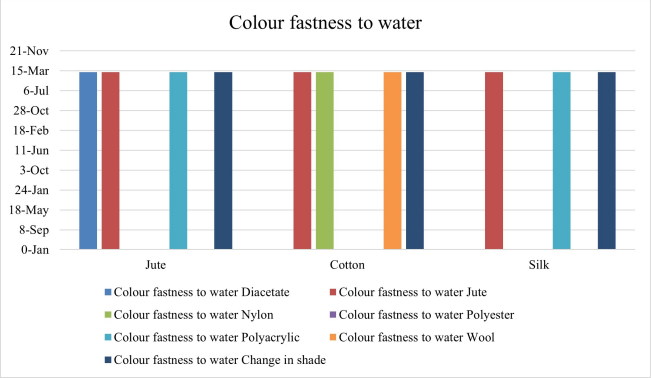

Figure 5: Color fastness to water

3.11. Change in shade for sea water

For all three of the materials treated using jamun bark dye, the color change was satisfactory (4-5).

3.12. Dry heat fastness

Jute and silk textiles performed well (4-5) during dry heat pressing at 110°C. In Table 3, results are displayed.

3.13. Color fastness to acidic and basic spotting

Jute's shade changes. Jute and silk fabrics received a satisfactory rating (4-5) after being spotted with acetic acid (300 g/l). For Jute and silk, Sulphuric acid (150 g/l) spotting yielded a rating of 4, while wool had an acceptable (3-4) rating. Alkali spotting (100 g/l Na_2CO_3) gave Jute and cotton fabrics an acceptable rating (3-4) while giving silk fabrics a rating of 4. The outcomes are listed in Table 3.

4. Conclusion

The study reveals that *Syzygium cumini* bark dye exhibits excellent to good color fastness properties. Its colors develop quickly and remain long-lasting. The dye can be applied to jute, cotton, and silk fibers without the use of a mordant and achieves satisfactory saturation. It is environmentally friendly and poses no health hazards.

Table 5: Walnut bark dye: Dry heat fastness, sporting to acids and alkalis and color fastness to water

Fabric	Dry heat fastness at 110 C	Acid spotting		Alkali spotting	Color fastness to water					
		Acetic acid (300 g/L)	Sulphuric acid (150 g/L)	Sodium carbonate (100 g/L)	Diacetate	Nylon	Polyester	Polyacrylic	Wool	Change in shade
Jute	4 - 5	4 - 5	4	3 - 4	4 - 5	4	5	4 - 5	4	4 - 5
Cotton	4 - 5	4 - 5	3 - 4	3	5	4 - 5	5	5	4 - 5	4 - 5
Silk	4 - 5	4 - 5	4	4	5	4	5	4 - 5	5	4 - 5

References

[1] S. Achrekar, G. Kaklij, M. Pote, S. Kelkar, Hypoglycemic activity of eugenia jambolana and ficus bengalensis: mechanism of action., In Vivo (Athens, Greece) 5 (2) (1991) 143–147.

[2] J. P. Maran, B. Priya, S. Manikandan, Modeling and optimization of supercritical fluid extraction of anthocyanin and phenolic compounds from syzygium cumini fruit pulp., Journal of Food Science and Technology-mysore 51 (9) (2014) 1938–1946. doi:10.1007/S13197-013-1237-Y.

[3] K. Migliato, Standardization of the extract of syzygium cumini (l.) skeels fruits through the antimicrobial activity, Caderno de Farmacia 21 (1) (2005) 55–56.

[4] R. Siva, Status of natural dyes and dye-yielding plants in india, Current science (2007) 916–925.

[5] A. K. Samanta, P. Agarwal, Application of natural dyes on textiles, Indian Journal of Fibre and Textile Research 34 (4) (2009) 384–399.

[6] R. Allen, Color Chemistry, Nelson, 1971.

[7] T. Bechtold, R. Mussak, Handbook of natural colorants, Vol. 8, John Wiley & Sons, 2009.

[8] P. S. Vankar, Handbook on natural dyes for industrial applications, National Institute of Industrial Re, 2007.

[9] B. Glover, J. H. Pierce, Are natural colorants good for your health?, Journal of the Society of Dyers and Colourists 109 (1) (1993) 5–7.

[10] E.-K. Hwang, Y.-H. Lee, H.-D. Kim, Dyeing, fastness, and deodorizing properties of cotton, silk, and wool fabrics dyed with gardenia, coffee sludge, cassia tora. l., and pomegranate extracts, Fibers and Polymers 9 (2008) 334–340.

[11] K. Hunger, Industrial dyes, 25 wiley (2003).

[12] S.-h. Kim, Dyeing characteristics and uv protection property of green tea dyed cotton fabrics: focusing on the effect of chitosan mordanting condition, Fibers and Polymers 7 (2006) 255–261.

[13] M. Allen, G. Bain, Measuring the uv protection factor of fabrics. retrieved march 25, 2008 (1994).

[14] A. K. Sarkar, An evaluation of uv protection imparted by cotton fabrics dyed with natural colorants, BMC dermatology 4 (2004) 1–8.

[15] K. Hoffmann, J. Laperre, A. Avermaete, P. Altmeyer, T. Gambichler, Defined uv protection by apparel textiles, Archives of Dermatology 137 (8) (2001) 1089–1094.

[16] D. Grifoni, L. Bacci, G. Zipoli, G. Carreras, S. Baronti, F. Sabatini, Laboratory and outdoor assessment of uv protection offered by flax and hemp fabrics dyed with natural dyes, Photochemistry and photobiology 85 (1) (2009) 313–320.

[17] H. AA, N. Ali, J. A. El-Thalouth, Green strategy for development of antimicrobial printed textile fabrics, Research Journal of Textile and Apparel 16 (1) (2012) 77–85.

[18] S. Han, Y. Yang, Antimicrobial activity of wool fabric treated with curcumin, Dyes and pigments 64 (2) (2005) 157–161.

[19] M. Khan, A. Omoloso, M. Kihara, Antibacterial activity of artocarpus heterophyllus, Fitoterapia 74 (5) (2003) 501–505.

[20] D. Gupta, S. K. Khare, A. Laha, Antimicrobial properties of natural dyes against gram-negative bacteria, Coloration Technology 120 (4) (2004) 167–171.

[21] G. Ke, W. Yu, W. Xu, Color evaluation of wool fabric dyed with rhizoma coptidis extract, Journal of Applied Polymer Science 101 (5) (2006) 3376–3380.

[22] M. Sudha, A. Saranya, G. Selvakumar, N. Sivakumar, Microbial degradation of azo dyes: a review, International Journal of Current Microbiology and Applied Sciences 3 (2) (2014) 670–690.

[23] T. Teklemedhin, L. Gopalakrishnan, Environmental friendly dyeing of silk fabric with natural dye extracted from cassia singueana, Plant. J Textile Sci Eng S 3 (2).

[24] A. H. Elbanna, E. A.-h. Mahrous, A. E.-S. Khaleel, T. S. El-alfy, Morphological and anatomical features of bauhinia vahlii wight & arnott. grown in egypt, Journal of Applied Pharmaceutical Science 6 (12) (2016) 084–093.

[25] R. Chavan, A. Kadam, Preliminary phytochemistry and antimicrobial activity of bark of bauhinia racemosa lamk.

[26] J. Guan, H. Lu, Y. Chen, Apparel performance of flame retardant silk fabrics, Journal of Engineered Fibers and Fabrics 8 (4) (2013) 155892501300800411.

[27] Q.-H. Zhang, W. Zhang, G.-Q. Chen, T.-L. Xing, Flame retardant finish of silk fabric with dimethyl phosphonate doped silica sol, in: 2nd Annual International Conference on Advanced Material Engineering (AME 2016), Atlantis Press, 2016, pp. 877–883.

[28] S. Basak, S. Chattopadhyay, S. Saxena, R. Narkar, et al., Banana pseudostem sap and boric acid-a new green intumescent for making self-extinguishing cotton fabric, Indian Journal of Fibre & Textile Research (IJFTR) 43 (1) (2018) 36–43.

Available online at www.rpnsci.com

Research Prospects in Natural Sciences Vol. 1, Issue 1, (2023) 15–18

Research Article

Study of Factors Effecting Growth Rate and Grain Density of Rubrene Deposited on Different Substrates Using Hot Wall Epitaxy

Kamila Rehman[a,b], Aaliya Rehman[a,*], Shaimaa M. abdalbaqi[b], Helmut Sitter[b]

[a]*Department of Physics, Govt. M.A.O. Graduate College, Lahore 54000, Pakistan*
[b]*Institute of Semiconductor Physics, Univeristy of Linz, 4040 Linz, Austria*

Abstract

Rubrene is a promising hydrocarbon for organic thin film transistors due to its remarkable carrier transport capabilities in the active semiconducting layer. Room temperature hole mobilities for single crystals have been high and are the reason for increased attention towards this material. In our work here we report on the thin films of rubrene deposited on two dielectric materials, SiO_2 and mica which resulted in nominal film thicknesses starting from sub monolayer. A study of island growth dependence on substrate temperatures has also been conducted. In order to understand the molecular growth dynamics of rubrene thin films on these two substrates, we made use of Atomic Force Microscopy for the characterization of these films and studied the pattern of island growth dependence on different substrate temperatures and substrates.

Keywords:
Hole mobility, Nominal film thickness.

1. Introduction

The field of optoelectronic devices using organic materials is gaining an increase in attention of researchers due to applications like organic field effect transistors (OFETs) [1, 2], photovoltaic cells [3] and light-emitting diodes (OLEDs) [4, 5]. One reason for this interest is the high performance of single crystal based OFETs using organic materials like rubrene (5,6,11,12-tetraphenyltetracene - $C_{42}H_{28}$) which have shown an interestingly high carrier mobility [6, 7]. The challenge, however, remains to achieve sufficiently high carrier mobilities using rubrene thin films as are seen for the single crystal-based devices [7–14].

Continuous attempts are being made to grow rubrene thin films of a crystalline nature, but results have showed spherulites which are small polycrystalline areas in the mostly amorphous films [15–17]. In order to fully understand the reason behind such a morphology, a detailed study of the different stages of thin film growth for rubrene is necessary. Research has been conducted into the initial stages of island formation [8–10, 16–28] and the consequent stage of coalescence and thin film development followed by the nucleation of crystalline areas namely spherulites [29]. Island formation of an amorphous nature on an amorphous wetting layer might be the most interesting stage of growth to be studied for the best understanding of morphology of rubrene thin films as it is followed by crystalline nucleation in between islands [30]. Here we put forward a similar study using substrates of mica and SiO_2 to see rubrene growth dependence on varying substrate temperatures.

2. Materials and Methods

Rubrene, an organic substance, was purchased from Aldrich and purified even further using thermal sublimation. The material was 98% pure. Rubrene was moved into the Hot Wall Epitaxy apparatus and placed in a quartz tube. Muscovite Mica substrates measuring $15\times15mm^2$ that were acquired from Segliwa GMBH were manually split fresh in the air before being placed in the HWE vacuum chamber. Subsequent to attaining a vacuum of 10-6 mbar, a 15-minute preheating process was conducted at the substrate deposition temperature. All materials that have been adsorbed onto the substrate surface are totally removed by this in situ heat treatment. Subsequently, at a vacuum

*Corresponding Author:
aaliya.rehman@gmail.com (Aaliya Rehman)

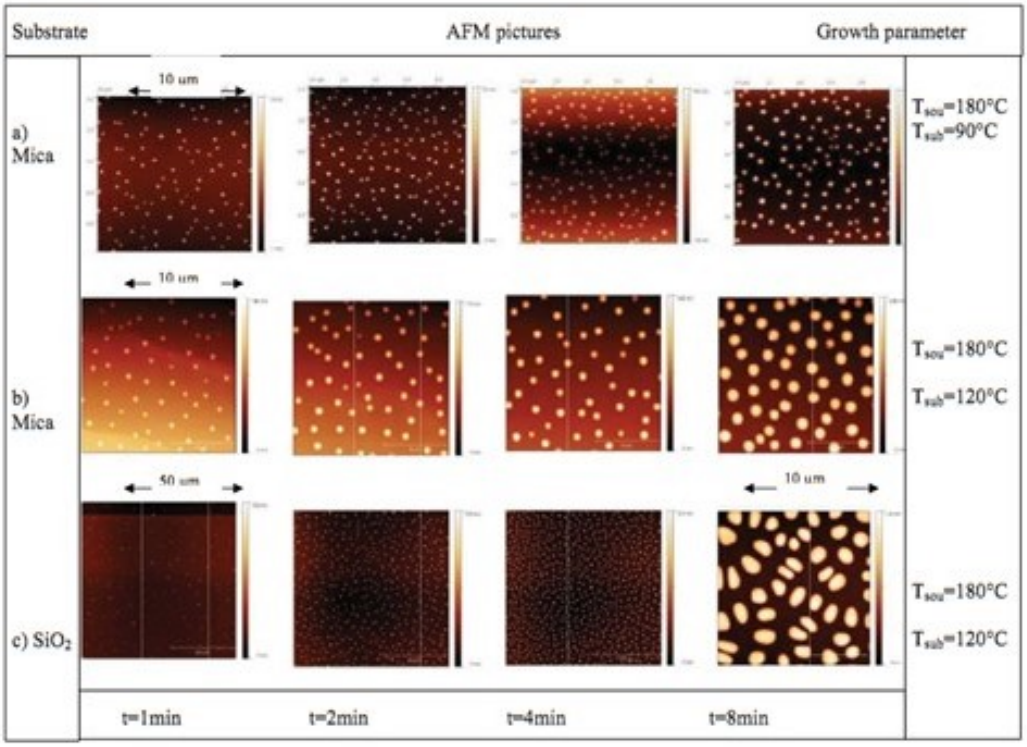

Figure 1. AFM images of rubrene grown on (a) mica surface at T_{sou} =180°C and T_{sub} = 90°C, (b) mica surface at T_{sou} =180°C and T_{sub} = 120°C and (c) SiO_2 surface at T_{sou} = 180°C and T_{sub} = 120°C, for growth times 1, 2, 4 and 8 minutes. The magnifications of images are (a) $10 \times 10\mu m^2$, (b) $10 \times 10\mu m^2$ and (c) $50 \times 50\mu m^2$.

of 10-6 mbar, rubrene was placed on mica (001) and recently cleaned SiO_2 wafer (SiO_2 coated Si wafer) substrates. The substrate temperatures that were utilised were 90°C and 120°C for mica and 120°C for SiO_2. In all situations, the wall temperature was maintained at 180°C in addition to the source temperature. The samples' growth times were 1, 2, 4, and 8 minutes. Using a SiC tip on regions measuring $10\times10\mu m^2$ and $50\times50\mu m^2$, morphology studies were conducted by acquiring atomic force microscopy (AFM) pictures of the deposited organic thin films using the tapping mode of a Digital Instruments Dimension 3100 microscope. These AFM images of rubrene placed on muscovite mica and SiO_2 substrates are displayed in Fig. 1. The following analysis was done on this set of AFM scans. To calculate the island density, one might count the number of grains per $10 \times 10\mu m^2$. The average height of these islands was determined by analyzing a significant number of cross sections, and this information was then utilized to calculate the distribution of island heights.

3. Results and Discussion

We obtained 98% pure rubrene from Aldrich which was further purified using thermal sublimation. Rubrene was deposited on freshly cleaved mica (001) and on freshly cleaned SiO_2 wafer substrates using hot wall epitaxy keeping substrate temperatures at 90°C and 120°C for mica and 120°C for SiO_2 at a vacuum of 10-6 mbar whereas the source temperature was maintained at 180°C for both cases. Digital Instruments Dimension 3100 in tapping mode was used to obtain AFM scans for morphology assessment as shown in Fig.1.

The nominal film thickness (NFT) was plotted versus growth time to find growth rate in each series of samples. Figures 2 and 3 show these plots of samples whose AFM scans are shown in Fig. 1. The results in Fig. 2 show a clear dependence of the amount of material deposited on the substrate temperature. Keeping the source temperature constant at 180°C the same number of molecules evaporated. The increased substrate temperatures in the first two series for mica increase the growth rate which can be attributed to greater diffusion lengths of rubrene molecules. Consequently, the nominal layer thickness was less at lower substrate temperatures. However, the grain count increase with time is prominent only at lower substrate temperature. The grain density is almost independent of growth time for the high substrate temperature while it increases in the beginning of growth at lower substrate temperatures and reaches a saturation. A similar comparison was made for samples grown at the same source and substrate temperatures but on different substrates of SiO_2 and mica. By performing the same evaluation procedure as described above, the results shown in Fig. 1 were obtained. The smaller growth rate for SiO_2 can be interpreted in terms of a smaller sticking coefficient of rubrene molecules on SiO_2 as compared to mica substrates. This assumption can also explain the increasing grain density on SiO_2. If the rubrene molecules cannot reach the next island within the time before they evaporate again only a small number of islands will be formed in the beginning. With increasing growth

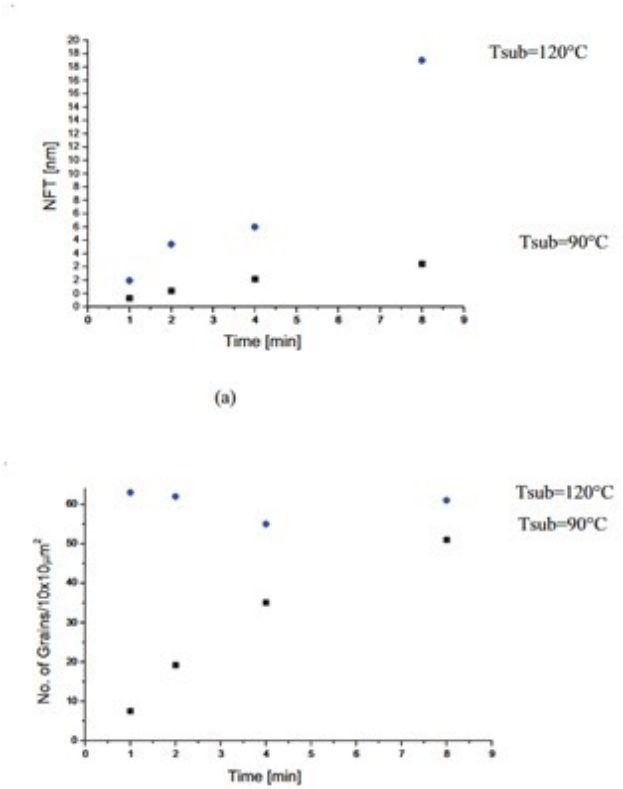

Figure 2. Comparison of (a) nominal film thickness (NFT) (b) grain count per $10 \times 10\mu m^2$ for samples prepared on mica at substrate temperature of 90°C and 120°C.

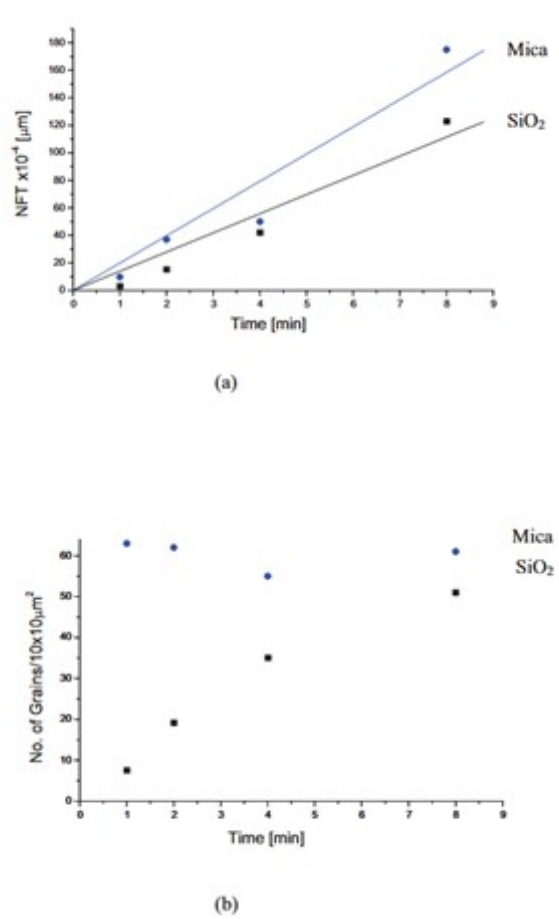

Figure 3. Comparison of (a) nominal film thickness (NFT) (b) grain count per $10 \times 10\mu m^2$ for samples prepared on mica and SiO_2 at source temperature of 180°C and substrate temperature of 120°C.

time more and more islands will provide stable positions for the rubrene molecules reducing the re-evaporation and resulting in an increased growth rate.

4. Conclusion

We have studied the early phases of growth of rubrene layers that are deposited on various substrates at varying substrate temperatures using Hot Wall Epitaxy. The findings indicate that whereas grain density is dependent on both substrate material and substrate temperature, thin film thickness at constant source temperature directly correlates with substrate temperature.

References

[1] A. Afzali, C. D. Dimitrakopoulos, T. O. Graham, Photosensitive pentacene precursor: synthesis, photothermal patterning, and application in thin-film transistors, Advanced Materials 15 (24) (2003) 2066–2069.

[2] M. Muccini, A bright future for organic field-effect transistors, Nature materials 5 (8) (2006) 605–613.

[3] P. Peumans, A. Yakimov, S. R. Forrest, Small molecular weight organic thin-film photodetectors and solar cells, Journal of Applied Physics 93 (7) (2003) 3693–3723.

[4] M. A. Baldo, D. F. O'Brien, Y. You, A. Shoustikov, S. Sibley, M. E. Thompson, S. R. Forrest, Highly efficient phosphorescent emission from organic electroluminescent devices, in: Electrophosphorescent Materials and Devices, Jenny Stanford Publishing, 2023, pp. 1–11.

[5] L. Hung, C. Chen, Recent progress of molecular organic electroluminescent materials and devices, Materials Science and Engineering: R: Reports 39 (5-6) (2002) 143–222.

[6] O. Mitrofanov, D. V. Lang, C. Kloc, J. M. Wikberg, T. Siegrist, W.-Y. So, M. Sergent, A. P. Ramirez, Oxygen-related band gap state in single crystal rubrene, Physical review letters 97 (16) (2006) 166601.

[7] V. C. Sundar, J. Zaumseil, V. Podzorov, E. Menard, R. L. Willett, T. Someya, M. E. Gershenson, J. A. Rogers, Elastomeric transistor stamps: reversible probing of charge transport in organic crystals, Science 303 (5664) (2004) 1644–1646.

[8] C. Hsu, J. Deng, C. Staddon, P. Beton, Growth front nucleation of rubrene thin films for high mobility organic transistors, applied physics letters 91 (19).

[9] S.-W. Park, J. M. Hwang, J.-M. Choi, D. Hwang, M. Oh, J. H. Kim, S. Im, Rubrene thin-film transistors with crystalline and amorphous channels, Applied physics letters 90 (15).

[10] S.-W. Park, S. Jeong, J.-M. Choi, J. M. Hwang, J. H. Kim, S. Im, Rubrene polycrystalline transistor channel achieved through in situ vacuum annealing, Applied Physics Letters 91 (3).

[11] V. Podzorov, V. Pudalov, M. Gershenson, Field-effect transistors on rubrene single crystals with parylene gate insulator, Applied physics letters 82 (11) (2003) 1739–1741.

[12] C. Goldmann, S. Haas, C. Krellner, K. Pernstich, D. Gundlach, B. Batlogg, Hole mobility in organic single crystals measured by a "flip-crystal" field-effect technique, Journal of Applied Physics 96 (4) (2004) 2080–2086.

[13] E. Menard, V. Podzorov, S.-H. Hur, A. Gaur, M. E. Gershenson, J. A. Rogers, High-performance n-and p-type single-crystal organic transistors with free-space gate dielectrics, Advanced materials 16 (23-24) (2004) 2097–2101.

[14] J. Takeya, M. Yamagishi, Y. Tominari, R. Hirahara, Y. Nakazawa,

T. Nishikawa, T. Kawase, T. Shimoda, S. Ogawa, Very high-mobility organic single-crystal transistors with in-crystal conduction channels, Applied Physics Letters 90 (10).

[15] H. Klauk, M. Halik, U. Zschieschang, G. Schmid, W. Radlik, W. Weber, High-mobility polymer gate dielectric pentacene thin film transistors, Journal of Applied Physics 92 (9) (2002) 5259–5263.

[16] C. Sheraw, L. Zhou, J. Huang, D. Gundlach, T. Jackson, M. Kane, I. Hill, M. Hammond, J. Campi, B. Greening, et al., Organic thin-film transistor-driven polymer-dispersed liquid crystal displays on flexible polymeric substrates, Applied physics letters 80 (6) (2002) 1088–1090.

[17] D. Käfer, L. Ruppel, G. Witte, C. Wöll, Role of molecular conformations in rubrene thin film growth, Physical review letters 95 (16) (2005) 166602.

[18] M. Campione, Rubrene heteroepitaxial nanostructures with unique orientation, The Journal of Physical Chemistry C 112 (42) (2008) 16178–16181.

[19] M. Haemori, J. Yamaguchi, S. Yaginuma, K. Itaka, H. Koinuma, Fabrication of highly oriented rubrene thin films by the use of atomically finished substrate and pentacene buffer layer, Japanese journal of applied physics 44 (6R) (2005) 3740.

[20] D. Käfer, G. Witte, Growth of crystalline rubrene films with enhanced stability, Physical Chemistry Chemical Physics 7 (15) (2005) 2850–2853.

[21] Y. Chen, I. Shih, High mobility organic thin film transistors based on monocrystalline rubrene films grown by low pressure hot wall deposition, Applied Physics Letters 94 (8).

[22] Y. Luo, M. Brun, P. Rannou, B. Grevin, Growth of rubrene thin film, spherulites and nanowires on sio2, physica status solidi (a) 204 (6) (2007) 1851–1855.

[23] P. R. Ribić, G. Bratina, Ripening of rubrene islands, The Journal of Physical Chemistry C 111 (50) (2007) 18558–18562.

[24] S. Kowarik, A. Gerlach, S. Sellner, F. Schreiber, J. Pflaum, L. Cavalcanti, O. Konovalov, Anomalous roughness evolution of rubrene thin films observed in real time during growth, Physical Chemistry Chemical Physics 8 (15) (2006) 1834–1836.

[25] G. Hlawacek, S. Abd-al Baqi, X. Ming He, H. Sitter, C. Teichert, Rubrene on mica: from the early growth stage to late crystallization, Interface Controlled Organic Thin Films (2009) 55–60.

[26] L. Gránásy, T. Pusztai, T. Börzsönyi, J. A. Warren, J. F. Douglas, A general mechanism of polycrystalline growth, Nature Materials 3 (9) (2004) 645–650.

[27] M. Brinkmann, S. Graff, F. Biscarini, Mechanism of nonrandom pattern formation of polar-conjugated molecules in a partial wetting regime, Physical review B 66 (16) (2002) 165430.

[28] Y. Kato, S. Iba, R. Teramoto, T. Sekitani, T. Someya, H. Kawaguchi, T. Sakurai, High mobility of pentacene field-effect transistors with polyimide gate dielectric layers, Applied physics letters 84 (19) (2004) 3789–3791.

[29] U. Stadlober, B Haas, A. Maresch, H Haase, Semiconductors ii: Surfaces, interfaces, microstructures, and related topics-growth model of pentacene on inorganic and organic dielectrics based on scaling and rate-equation theory, Physical Review-Section B-Condensed Matter 74 (16) (2006) 165302–165302.

[30] H. Zaglmayr, L. Sun, G. Weidlinger, S. M. Abd Al-Baqi, H. Sitter, P. Zeppenfeld, Initial stage of crystalline rubrene thin film growth on mica (0 0 1), Synthetic metals 161 (3-4) (2011) 271–274.

Available online at www.rpnsci.com

Research Prospects in Natural Sciences Vol. 1, Issue 1, (2023) 19–24

Research Article

A DFT STUDY OF STRUCTURAL AND ELECTRONIC PROPERTIES OF SPINEL FERRITE $CdFe_2O_4$

Muhammad Aslam Dar[a,b,*], Farhan Ahmad[a,c], Muhammad Ashraf[a,c], Amin Ur Rehman[b]

[a] *Higher Education Department, Government of Punjab, Lahore 54000, Pakistan.*
[b] *University of the Lahore, Lahore 54000, Punjab, Pakistan.*
[c] *Department of Solid State Physics, University of the Punjab, Lahore 54000, Pakistan.*

Abstract

A density functional theory (DFT) study of structural and electronic properties of Spinel ferrite $CdFe_2O_4$ is done here by using computer code WIEN2k. Structural characteristics like lattice constant, bulk modulus, ground state volume and ground state energy are determined by using exchange correlation approximations LDA, PBE-GGA and WC-GGA. Lattice constant measured by PBE-GGA is agreed well with the experimental results. All three types of approximations reveal that $CdFe_2O_4$ has simple cubic structure. Density of States (DOS) and band structure are determined by using Full Potential Linearized Augmented Plane Wave (FP-LAPW) method within generalized gradient approximation PBE-GGA. The values of lattice constant, ground state energy and bulk modulus using the approximations PBE-GGA are 8.7030 Å-33770.2312 Ry and 168.7308 GPa, respectively. Total density of states (TDOS) and partial density of states (PDOS) are determined for both spin-up and spin-down. Energy band gap (1.2 eV) shows that Cadmium Ferrite has half metallic nature and has indirect band gap. Cadmium Ferrite is low gap semiconductors and widely used in electronics such as in magnetic and magneto-optic recording devices and in data storage devices. This work provides first comprehensive DFT study to understand the properties of Cadmium Ferrite ($CdFe_2O_4$) with LDA, PBE-GGA and WC-GGA.

Keywords:
DFT, DOS, PDOS, cadmium ferrite.

1. Introduction

Ferrites are generally has resistivity in between those of conductors and insulators. Electronic properties of ferrites have made them more attractive and interesting for both scientists and engineers. These properties of ferrites have made them able to play an important role in manufacturing of magnetic switches, transformer cores, microwave devices, micro electric devices, sensors, electromagnetic circuits and in the field of medicines [1, 2]. General Formula for spinel ferrites is MFe_2O_4, here M is a divalent metal ion e.g., Magnesium ($_{12}$Mg), Manganese ($_{25}$Mn), Nickel ($_{28}$Ni), Copper ($_{29}$Cu), Cadmium ($_{48}$Cd) etc., Fe is cation (+ve ion) and O is an anion (-ve ion). Spinel ferrites have simple cubic structure, their space group is 227 ($Fd\bar{3}m$) [3]. Lattice constant for spinel ferrites is about 8.38 Å and their curie temperature is 668 K. Resistivity of spinel ferrites is about $1\times106\ \Omega$ m. The crystal structure of spinal ferrites is cubic and has two interstitial sites called tetrahedral site and octahedral site. Each unit cell of spinel ferrites consist of eight units (cube) and therefore written as $M_8Fe_{16}O_{32}$. Bragg and Nishikawa were the first who determined the cubic structure of spinel ferrites [4].

Among all types of ferrites spinel-ferrites are very important because of their wide range of applications in many fields. Spinel ferrites are very useful materials for magnetic recording media and computer memory devices. They are also used in components of magnetic switches, electronic filters and microwave devices. For memory and switching devices they are used in form of thin films. They are extensively used in manufacturing of rod antenna and radio frequency coil [5, 6]. Spinel ferrites are used to make sensors which have definite and sharp Curie temperature and can be used for temperature control. These ferrites can also be used for humidity sensitivity, they have large surface area, open pore formed on bulk surface and have high surface charge density [7, 8].

$CdFe_2O_4$ is an important spinel ferrite, it has many applica-

*Corresponding Author:
aslamdar83@gmail.com (Muhammad Aslam Dar)

tions in bulk form as well as in nanoparticle form. $CdFe_2O_4$ is a semiconductor oxide. It has an ability to resolve the many environmental and energy problems. $CdFe_2O_4$ can use solar energy to eliminate serious pollutants in air as well as in water, it can also effectively detect toxic gases in atmosphere of Earth and can protect the living organisms from harmful impacts of various pollutants present in our surrounding[9, 10]. $CdFe_2O_4$ is a normal spinel ferrite and like other ferrites it also shows magnetic properties[11]. $CdFe_2O_4$ in bulk form shows ferromagnetic properties but below 10K it shows antiferromagnetic behavior [12]. Cadmium ferrite ($CdFe_2O_4$) has a number of electronic, magnetic, catalytical and electrical switching properties. $CdFe_2O_4$ has cubic structure belonging to space group 227 i.e. Fd3m. In Cadmium ferrite Cd is tetrahedral cation, Fe is octahedral cation, here the unit cell dimensions (Lattice Constant) a = 8.7050Å, anion positional parameter ucalc = 0.2685Å, tetrahedral bond length R_{tet} = 0.780Å, octahedral bond length R_{oct} = 0.645Å, electronegativity of tetrahedral cation χ_{tet} = 1.690, electronegativity of octahedral cation χ_{oct} = 1.830 [13]. In bulk form $CdFe_2O_4$ has X- ray density ρ = 5.81x 103 Kg m-3, force constant K=1.00 x102 Nm-1 , bulk modulus B = 206 GPa , young modulus E = 185 GPa , rigidity modulus G = 68 GPa , PoissonÂ´s ratio σ = 0.35 , Debye temperature θ = 499 k [14]. Experimentally it is noted that Cadmium ferrite has conductivity in between the conductors and insulators, at standard temperature the experimental values of band energies for $CdFe_2O_4$ are given as, conduction band energy ECB = 0.55 eV , valance band energy EVB = 2.85 eV, energy band gap Eg = 2.3 eV, these values show that Cadmium ferrite is electrically semiconductor material [15]. This research is an attempt to find out structural and electronic properties of spinel ferrite $CdFe_2O_4$ based on DFT and then compares them with already existing experimental results.

2. Materials and Methods

Density Functional Theory is the theoretical tool to investigate solids by finding the density of electrons in the material. DFT is an ab-initio method to solve the Schrodinger equation for many body problems. In this theoretical technique a number of suitable approximations are made to solve the Schrodinger equation and an attempt is made to reach to the reasonable suitable results of the given materials. The first step to solve Schrodinger wave equation for complex matter is the Born-Oppenheimer approximation. This approximation separates the motion of nuclei and the electrons. Hartree proposed that Schrodinger equation for many electron system can be rewrite as a single-electron equation, and this electron is considered as moving in a mean potential from all the other electrons. According to Hartree-Fock approximation the exact wave function of many-body system needs to be anti-symmetric function by exchange of electrons. InHartree-Fock technique the exchange is treated exactly but the correlation is ignored [16, 17].

DFT is based on charge density of electrons rather than wave function of electrons, i.e., $E(\Psi_\circ) = E(\rho_\circ)$. DFT is a successful and an efficient technique to investigate a solid. It is the most reliable method to find the properties of condensed matter. It is the theory which reduced the many-particle Schrodinger equation to single-body independent Schrodinger equation. Modern DFT found its roots in 1964 AD by Hohenberg and Kohn. They gave two landmarks theorems which provided a base to investigate a material theoretically by using DFT [18]. Kohn and Sham played an important role to make DFT more suitable to measure the exact value of electron density. By applying the Kohn-Sham ideas the single electrons equations are formed. These single electrons Schrodinger equations are known as Kohn-Sham equations. i.e.

$$\widehat{H}_{KS}\Phi_i = \left[-\frac{1}{2}\nabla^2 + V_{eff}\left[\rho\left(\overrightarrow{r}\right)\right]\right]\Phi_i\left(\overrightarrow{r}\right) \quad (1)$$

Here $\widehat{H}_{KS}$ is single electron Hamiltonian and $V_{eff}(r)$ is effective potential formed by all other electrons in which single electron moves. This effective potential can be written as,

$$V_{eff}\left[\rho\left(\overrightarrow{r}\right)\right] = V_{ext}\left(\overrightarrow{r}\right) + \widehat{V}_H\left[\rho\left(\overrightarrow{r}\right)\right] + V_{xc}\left[\rho\left(\overrightarrow{r}\right)\right] \quad (2)$$

The Kohn-Sham equations are needed to be solved self-consistently. An initial charge density is supposed and then by using this initial guessed the Hamiltonian for this charge density is set up and then diagonalized the resulting approximate Hamiltonian. The main purpose of Kohn-Sham theory is to find the exact results for many-body system by making reasonable approximations to calculate $\frac{E_{xc}}{V_{xc}}$ [19].

Here in these calculations we used three different approximations LDA, PBE-GGA and WC-GGA to find the structural and electronic properties of $CdFe_2O_4$. WIEN2k is a computer software which is being used here, WIEN2k works on the bases of DFT [20, 21]. WIEN2k is an excellent scheme to find out the structural, electrical, magnetic, optical and elastic properties of solid materials. The computer code WIEN2k is followed the method of Full Potential Augmented Plane-Wave (APW) + local orbitals (Lo). Here in this method the crystal unit cell is divided into two main regions, one is non-overlapping Muffin-Tin sphere and the second is the remaining interstitial space. WIEN2k is an all electrons method, it can made calculations for valance electrons and also for the core electrons [22].

3. Results and Discussion

3.1. Structural Properties

Structural properties of Spinel ferrite $CdFe_2O_4$ is determined here by using Density Functional Theory (DFT), structural properties is characterized by finding some important parameters such as lattice constant, bulk modulus, minimum volume, minimum energy and the pressure derivative of bulk modulus. These structural parameters are determined at different potentials by using LDA, PBE-GGA and WC-GGA. To determine the ground state energy for these two compounds, their total energy is minimized at various volumes by using the Murnaghan's equation of state [23] which can be given as,

$$E(V) = E_\circ + \frac{9V_\circ B_\circ}{16}\left[\left\{\left(\frac{V_\circ}{V}\right)^{\frac{2}{3}} - 1\right\}^2 B'_\circ + \left\{\left(\frac{V_\circ}{V}\right)^{\frac{2}{3}} - 1\right\}^2 \left\{6 - 4\left(\frac{V_\circ}{V}\right)\right\}^{\frac{2}{3}}\right] \quad (3)$$

Here $B'_\circ$ is the pressure derivative of bulk modulus $B_\circ$ and it is given as,

$$B'_\circ = \frac{dB_\circ}{dP} \tag{4}$$

Where $E_\circ$ is the minimum energy and $V_\circ$ is the minimum volume By taking minimum energy the graphs are drawn between total energy and the volume for all three approximations i.e. LDA, PBE-GGA and WC-GGA. In each case approximations having values of structural parameters nearly equal to that of experimental values are selected. Our calculated structural parameters by using PBE-GGA are completely agreed with experimental values. Atomic positions of cadmium (Cd), iron (Fe), and oxygen (O) in Cadmium ferrite which are used to calculate the optimized lattice constants are given in table 1. Each unit cell of optimized $CdFe_2O_4$ crystal is cubical belonging to space group 227 (Fd3m), cubical crystal structure of $CdFe_2O_4$ is shown in figure 1.

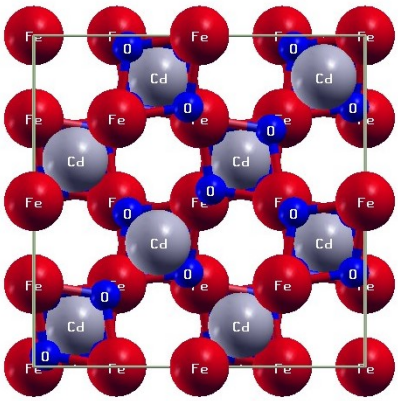

Figure 1: Crystal structure of $CdFe_2O_4$

By using Local Density Approximation (LDA) calculated ground state energy is $E_\circ$ = -33725.3212 Ry, minimum optimum volume is $V_\circ$=1034.4154 a.u3, the stiffness of the material (Bulk Modulus) is B = 214.1811 GPa, the pressure derivative of bulk modulus is BP = 5.0000. Calculated Lattice Parameters by LDA and relative % error by comparing with experimental data is shown table 2. Optimized curve volume vs energy for CdFe2O4 by using LDA is shown in figure 2.

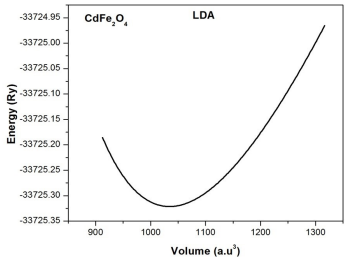

Figure 2: Volume vs Energy Plot for $CdFe_2O_4$ within LDA

By using PBE-GGA calculated ground state energy is $E_\circ$ = -33770.2312 Ry, minimum optimum volume is $V_\circ$= 1112.1083 a.u3, the stiffness of the material (Bulk Modulus) is B = 168.7308 GPa, the pressure derivative of bulk modulus is BP = 5.0000. Calculated Lattice Parameters by PBE-GGA and relative % error by comparing with experimental data is shown table 3. Optimized curve volume vs energy for $CdFe_2O_4$ by using PBE-GGA is shown in figure 3.

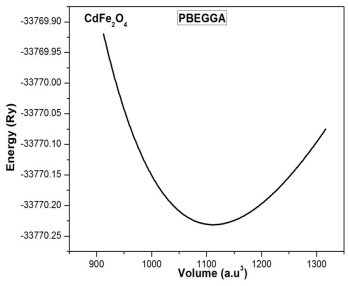

Figure 3: Volume vs Energy Plot for $CdFe_2O_4$ within PBE-GGA

By using WC-GGA calculated ground state energy is $E_\circ$= -33762.4552 Ry, minimum optimum volume is $V_\circ$ =1071.3152 a.u3, stiffness of the material (Bulk Modulus) is B = 181.9959 GPa, the pressure derivative of bulk modulus is BP = 5.0000. Calculated Lattice Parameters by WC-GGA and relative % error by comparing with experimental data is shown table 4. Optimized curve volume vs energy for $CdFe_2O_4$ by using WC-GGA is shown in figure 4.

Table 1: Atomic positions for $CdFe_2O_4$

Atoms	X	Y	Z
Cd	0.125	0.125	0.125
Fe	0.5	0.5	0.5
O	0.2847	0.2847	0.2847

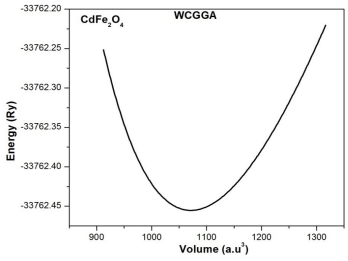

Figure 4: Volume vs Energy Plot for $CdFe_2O_4$ within WC-GGA

3.2. Electronic Properties

In complex matter physics the density of states (DOS) of a material are described as, “number of states per interval of

Table 2: Calculated Lattice Parameters by LDA for $CdFe_2O_4$

Lattice parameter	Calculated values	Experimental Data [14]	% Error
Lattice Constant $a_\circ$(Å)	8.4954	8.7000	2.35
Minimum Volume $V_\circ(a.u^3)$	1034.4154	1033.215	0.12
Minium energy $E_\circ(Ry)$	-33725.3212	-33720.416	0.014
Bulk Modulus B (GPa)	214.1811	206	3.97
BP	5.000	5.000	0.0

Table 3: Calculated Lattice Parameters by PBE-GGA for $CdFe_2O_4$

Lattice parameter	Calculated values	Experimental Data [14]	% Error
Lattice Constant $a_\circ$(Å)	8.7030	8.7000	0.034
Minimum Volume $V_\circ(a.u^3)$	1112.1083	1033.215	7.6
Minium energy $E_\circ(Ry)$	-33770.2312	-33720.416	0.15
Bulk Modulus B (GPa)	168.7308	206	18.09
BP	5.000	5.000	0.0

energy at each energy level available to the occupied". In crystalline structure of a material electron waves can propagate only in one direction i.e. only certain states are permitted. Therefore it can be possible that in any specific energy level a number of states are available for occupation and on another energy level it can also be possible that no states are available. In three dimensional system the units of DOS is Energy-1 Volume-1 , in two dimensional system units of DOS is Energy-1 Area-1 , in one dimensional system the units of DOS is Energy-1 Length-1 [24].

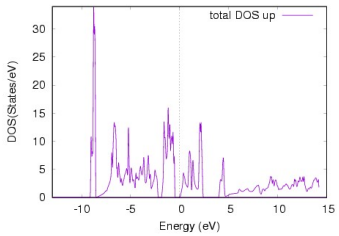

Figure 5: TDOS of $CdFe_2O_4$ for up spin within PBE-GGA

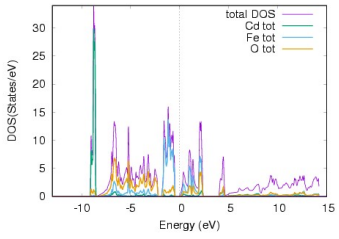

Figure 6: TDOS of $CdFe_2O_4$ for down spin within PBE-GGA

We computed total density of states (TDOS) and partial density of states (PDOS) for $CdFe_2O_4$ crystal by using exchange correlation approximation PBE-GGA. Total density of states for spin up and spin down are shown in figures 5 and 6 respectively. TDOS for spin up shows that band gap calculated by PBE-GGA corresponds to three parts in valance band of energy range -9.2 eV -8.4 eV, -8.2 eV 3.0 eV and -1.8 eV -0.4 eV.

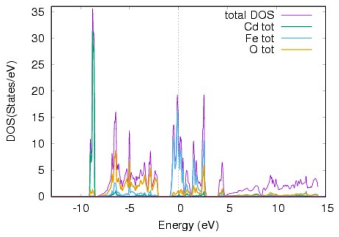

Figure 7: PDOS of $CdFe_2O_4$ for up spin within PBE-GGA

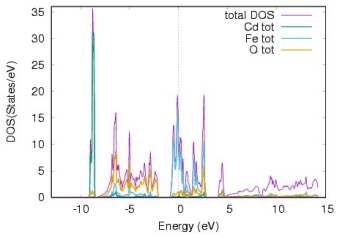

Figure 8: PDOS of $CdFe_2O_4$ for down spin within PBE-GGA

In valance band region the energy range -9.2 eV -8.4 eV has DOS value 38, -8.2 eV 3.0 eV has DOS value 13.5 and -1.8 eV -0.4 eV has DOS value 16. Highest valance band peak occurs in region -9.2 eV -8.4 eV. Total density of states (TDOS) of CdFe2O4 for up-spin within PBE-GGA shows that conduction band corresponds to 0 eV 2.5 eV, 4.2 eV 4.8 eV and 5.0 eV 14.2 eV. In conduction band region the energy range 0 eV 2.5 eV has DOS value 13.8, energy range 4.2 eV 4.8 eV has DOS value 7.6 and 5.0 eV 14.2 eV has DOS value

Table 4: Calculated Lattice Parameters by WC-GGA for $CdFe_2O_4$

Lattice parameter	Calculated values	Experimental Data [14]	% Error
Lattice Constant $a_\circ$(Å)	8.5953	8.7000	1.20
Minimum Volume $V_\circ(a.u^3)$	1071.3152	1033.215	3.7
Minium energy $E_\circ(Ry)$	-33762.2312	-33720.416	0.12
Bulk Modulus B (GPa)	181.9959	206	11.6
BP	5.000	5.000	0.0

4. Highest peak in conduction band region is occurred between 0 eV 2.5 eV. Partial density of states (PDOS) of Cadmium Ferrite ($CdFe_2O_4$) for spin up and spin down within PBE-GGA are shown in figures 7 and 8 respectively.

PDOS for spin up shows that on valance band region the contribution made by Cadmium (Cd) is from -9.2 eV to -8.4 eV at DOS value 30 and Cd contributes on conduction band side from 0 eV to 2.5 eV at DOS value 1.2. Contribution made by Fe in valance band region is from -7.6 eV to -2.2 eV at DOS value 3 and from -1.8 eV to -0.4 eV at DOS value 14. Fe has its contribution in conduction band region from 0 eV to 2.5 eV at DOS value 8. Oxygen (O) contribute from -9.2 eV to -8.4 eV at DOS value 1.5, from -8.0 eV to -3.0 eV at DOS value 6.5 and from -1.8 eV to 0.4 eV at DOS value 2 in valance band region. O made contribution from 0 eV to 2.5 eV at DOS value 4.5 and from 4.2 eV to 4.8 eV at DOS value 2 in conduction band region.

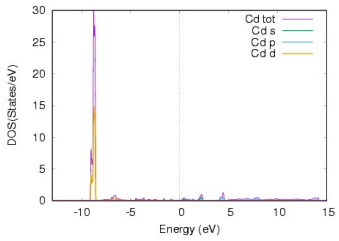

Figure 9: PDOS of Cd-atom for up spin within PBE-GGA

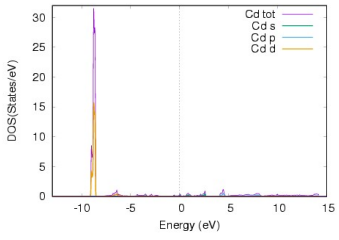

Figure 10: PDOS of Cd-atom for down spin within PBE-GGA

In total density of states (TDOS) the highest peak in valance band region with DOS value 38 is mainly contributed by Cadmium Cd-4d. In valance band region from -8.2 eV to 3.0 eV at DOS value 13.5 is contributed by Oxygen O-2p and similarly third range in valance band from -1.8 eV to 0.4 eV with DOS value 16 is mainly contributed by Fe-3d. In conduction band the highest peak with DOS value 13.8 from 0 eV to 2.5 eV is contributed by both Fe-3d and O-2p. Partial density of states (PDOS) for Cd, Fe, and Oxygen with spin up and spin down are shown in figures 9-14.

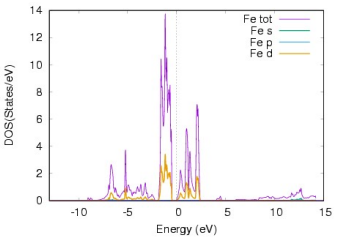

Figure 11: PDOS of Fe-atom for up spin within PBE-GGA

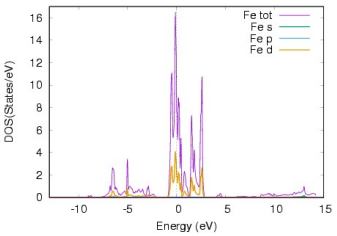

Figure 12: PDOS of Fe-atom for down spin within PBE-GGA

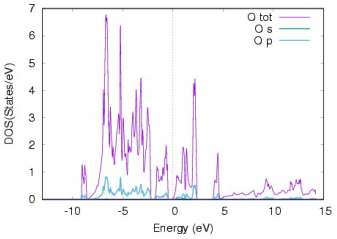

Figure 13: PDOS of O-atom for up spin within PBE-GGA

Band gap calculations for $CdFe_2O_4$ is calculated by using the exchange correlation approximation PBE-GGA between the energy range -10.0 eV to 8.0 eV. Band gap for $CdFe_2O_4$ for up-spin and down-spin within PBE-GGA are shown in figures 15

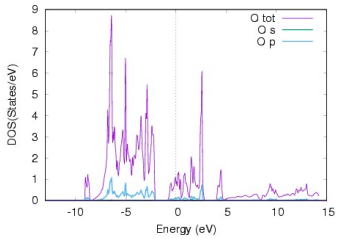

Figure 14: PDOS of O-atom for down spin within PBE-GGA

and 16 respectively. In our calculations it is found that Cadmium Ferrite has indirect band gap structure. Band structure of $CdFe_2O_4$ for up-spin shows a band gap of about 1.2 eV but for down-spin valance band and conduction band overlap each other showing zero band gap. This predicted that Cadmium Ferrite ($CdFe_2O_4$) is semiconductor in nature. At $0^{\circ}C$ or at 273K experimental value for $CdFe_2O_4$ band gap is about 2.3 eV [15].

4. Conclusion

WIEN2k computer code is used here, it applies the Full Potential Linearized Augmented Plane Wave (FP-LAPW) method within DFT. Structural parameters such as lattice constant, bulk modulus, ground state volume and ground state energy are determined here by using three exchange correlation potentials LDA, PBE-GGA and WC-GGA. Results obtained here by using DFT are agreed with experimental results especially with PBE-GGA. These calculations show that $CdFe_2O_4$ has simple cubic structure and here Cadmium (Cd) is tetrahedral cations, and Iron (Fe) is octahedral cation. The values obtained by PBE-GGA are as follows; lattice constant 8.7030 Å, minimum volume 1112.1083 $a.u^3$, minimum energy $E_{\circ}$ -33770.2312 Ry and bulk modulus B 168.7308 GPa. PBE-GGA is used here to find the total density of states (TDOS), partial density of states (PDOS) and electronic band structure for both spin-up and spin-down. Electronic band structure for Cadmium Ferrite is indirect band gap and shows some band gap for spin-up (of about 1.2 eV), but for spin-down valance band and conduction band overlap each other (zero band gap). This shows that $CdFe_2O_4$ has semi metallic nature. This is the first ab-initio study of electronic band structure of spinel ferrite $CdFe_2O_4$ with PBE-GGA.

References

[1] R. Bhowmik, N. Naresh, Structure, ac conductivity and complex impedance study of co3o4 and fe3o4 mixed spinel ferrites, International journal of Engineering, science and technology 2 (8).

[2] I. Chicinas, Soft magnetic nanocrystalline powders produced by mechanical alloying routes, Journal of Optoelectronics and Advanced Materials 8 (2) (2006) 439.

[3] E. Whittaker, (rwg) wyckoff crystal structures. vol. 2. 2nd edn, new york, london, sydney (interscience publishers), 1964. viii+ 588 pp. illus. price: 180s., Mineralogical magazine and journal of the Mineralogical Society 35 (271) (1965) 554–555.

[4] W. H. Bragg, Xxx. the structure of the spinel group of crystals, The London, Edinburgh, and Dublin Philosophical Magazine and Journal of Science 30 (176) (1915) 305–315.

[5] Y. He, S. Wang, C. Li, Y. Miao, Z. Wu, B. Zou, Synthesis and characterization of functionalized silica-coated fe3o4 superparamagnetic nanocrystals for biological applications, Journal of Physics D: Applied Physics 38 (9) (2005) 1342.

[6] M. Meshram, N. K. Agrawal, B. Sinha, P. Misra, Characterization of m-type barium hexagonal ferrite-based wide band microwave absorber, Journal of Magnetism and Magnetic Materials 271 (2-3) (2004) 207–214.

[7] R. Kotnala, J. Shah, B. Singh, S. Singh, S. Dhawan, A. Sengupta, et al., Humidity response of li-substituted magnesium ferrite, Sensors and Actuators B: Chemical 129 (2) (2008) 909–914.

[8] S. L. C. J. M. H. M. S. Pederson, S. Morup, Journal of physics: condensed matter 9 (71).

[9] E. Serrano, G. Rus, J. Garcia-Martinez, Nanotechnology for sustainable energy, Renewable and Sustainable Energy Reviews 13 (9) (2009) 2373–2384.

[10] S. Sun, X. Chang, L. Dong, Y. Zhang, Z. Li, Y. Qiu, W18o49 nanorods decorated with ag/agcl nanoparticles as highly-sensitive gas-sensing material and visible-light-driven photocatalyst, Journal of Solid State Chemistry 184 (8) (2011) 2190–2195.

[11] H. H. Hamdeh, J. Ho, S. Oliver, R. Willey, G. Oliveri, G. Busca, Magnetic properties of partially-inverted zinc ferrite aerogel powders, Journal of Applied Physics 81 (4) (1997) 1851–1857.

[12] V. Šepelák, K. Tkáčová, A. Rykov, Rietveld analysis of mechanically activated powdered zinc ferrite, Crystal Research and Technology 28 (1) (1993) 53–56.

[13] R. J. Hill, J. R. Craig, G. Gibbs, Systematics of the spinel structure type, Physics and chemistry of minerals 4 (4) (1979) 317–339.

[14] R. Desai, R. Mehta, R. Upadhyay, A. Gupta, A. Praneet, K. Rao, Bulk magnetic properties of cdfe 2 o 4 in nano-regime, Bulletin of Materials Science 30 (2007) 197–203.

[15] Y. Xu, M. A. Schoonen, The absolute energy positions of conduction and valence bands of selected semiconducting minerals, American mineralogist 85 (3-4) (2000) 543–556.

[16] S. Cottenier, et al., Density functional theory and the family of (l) apw-methods: a step-by-step introduction, Instituut voor Kern-en Stralingsfysica, KU Leuven, Belgium 4 (0) (2002) 41.

[17] [link].
URL http://en.wikipedia.org/wiki/Hartree-Fock

[18] P. Hohenberg, W. Kohn, Inhomogeneous electron gas, Physical review 136 (3B) (1964) B864.

[19] M. Städele, M. Moukara, J. Majewski, P. Vogl, A. Görling, Exact exchange kohn-sham formalism applied to semiconductors, Physical Review B 59 (15) (1999) 10031.

[20] P. Blaha, K. Schwarz, G. K. Madsen, D. Kvasnicka, J. Luitz, et al., wien2k, An augmented plane wave+ local orbitals program for calculating crystal properties 60 (2001) 1–302.

[21] K. Schwarz, P. Blaha, Solid state calculations using wien2k, Computational Materials Science 28 (2) (2003) 259–273.

[22] P. E. Blöchl, O. Jepsen, O. K. Andersen, Improved tetrahedron method for brillouin-zone integrations, Physical Review B 49 (23) (1994) 16223.

[23] F. D. Murnaghan, On the theory of the tension of an elastic cylinder, Proceedings of the National Academy of Sciences USA 30 (12) (1944) 5390.

[24] F. Wang, D. P. Landau, Efficient, multiple-range random walk algorithm to calculate the density of states, Physical review letters 86 (10) (2001) 2050.

Available online at www.rpnsci.com

Research Prospects in Natural Sciences Vol. 1, Issue 1, (2023) 25–31

Research Article

Electromagnetic wave propagation in a parallel-plate waveguide filled with linear metamaterials

Burhan Zamir[a,*], Aqib Nisar[b], Babar Shahzad[b]

[a]*Department of Physics, Govt. M. A. O. Graduate College, Lahore 54000, Pakistan*
[b]*Department of Physics, Division of Science & Technology, University of Education, Lahore 54700, Pakistan.*

Abstract

In this article, we present an analysis of electromagnetic wave propagation in a parallel-plate waveguide filled with (a) a conventional (linear, homogeneous and isotropic) dielectric medium (b) metamaterial. In this connection, we derive the dispersion relations for the TE and TM wave modes for both cases. The dispersion characteristics of the waves are obtained by the numerical analysis of the dispersion relation by plotting it for the propagation frequency versus the wave vector for different values of the dimensions of the waveguide and the number of modes. The dispersion characteristics show propagation and non-propagation regions in the microwave frequency range. This effect can be used for different waveguide applications e.g., filters, sensors etc.

Keywords:
Wave propagation, Parallel-plate waveguide, metamaterials.

1. Introduction

In recent years, the field of metamaterials (MTMs) has garnered significant attention due to their unique electromagnetic properties that can be tailored for specific applications [1–5]. One of the most promising applications of metamaterials is in the design of waveguides for high-frequency communication systems [6–10]. Metamaterials are engineered materials with unique electromagnetic properties that are not found in natural materials. They are designed by arranging subwavelength building blocks in a specific pattern to achieve the desired properties. Metamaterials can exhibit unusual properties such as negative refraction, cloaking, and super-resolution, which have potential applications in various fields including telecommunications [11–14]. The well-known types of metamaterials are double negative (DNG) and single negative (SNG) metamaterials. Double negative metamaterials (DNG-MTMs), also known as left-handed metamaterials [15, 16], consist of a composite of two materials, one with negative permittivity and the other with negative permeability. The idea of left-handed metamaterials was developed theoretically by Veselago [16] in 1968. Later, Pendry et al. [17–19], Smith et al. [20], and Shelby et al. [21] experimentally realized the artificial negative permittivity and permeability by constructing a composite medium in microwave frequency band based on a periodic array of interspaced conducting split-ring resonators and long continuous metallic wires. This combination results in a negative refractive index and allows light to propagate in a direction opposite to that in natural materials. Single negative metamaterials (SNG-MTMs) are categorized in two categories, the materials with negative permittivity and positive permeability are termed as the epsilon negative metamaterials (ENG-MTMS), whereas materials with positive permittivity and negative permeability are called mu-negative metamaterials (MNG-MTMs). SNG-MTMs are typically easier to fabricate than double negative metamaterials, and they have potential applications [22, 23].

Parallel-plate waveguides (PPWGs) are a common type of waveguide used in the transmission of electromagnetic waves. By filling the PPWG with a metamaterial, the propagation of the waves can be controlled and manipulated in ways not possible with conventional materials. This has opened up new possibilities for the design of waveguides with improved performance (see e.g. [22] and references therein). In recent years, some research work is reported for the high-frequency electro-

*Corresponding Author:
burhanzamir1@gmail.com (Burhan Zamir)

magnetic wave propagation in MTM based waveguides [6–15]. In this connection, Zamir and Ali [24] investigated the change in propagation properties of a nonlinear MTM filled PPWG by replacing the perfect-conducting plates to high- temperature superconductor parallel plates. They reported some new and different aspects of the wave propagation properties which were not present in a conventional PPWG. In this research paper, we will theoretically investigate the propagation properties of a parallel-plate waveguide filled with linear metamaterials and explore the potential applications of this technology in high-frequency communication systems.

2. Theoretical analysis

In this paper, we study the electromagnetic wave propagation in a PPWG filled with linear MTMs. A schematic representation of the proposed waveguide structure is shown in Figure (1). Consider an electromagnetic wave is propagating through a parallel-plate waveguide loaded with a DNG-MTM along z-axis with profile $e^{i(\omega t-kz)}$, as shown in Figure (1). Here, ω is the propagation frequency of the electromagnetic wave and k is the propagation constant. The parallel-plates are extended infinitely in yz-plane, whereas the separation between the plates id a.

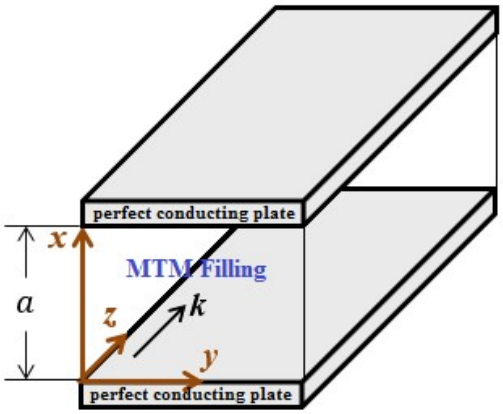

Figure 1: A PPWG filled with linear MTMs

A DNG-MTM is characterized by its simultaneously negative permittivity and permeability in a certain range of propagation frequency, given by the following relative functions:

$$\varepsilon_{_{DNG}}(\omega) = 1 - \frac{\omega_p^2}{\omega^2} \tag{1}$$

$$\mu_{_{DNG}}(\omega) = 1 - \frac{F\omega^2}{\omega^2 - \omega_r^2} \tag{2}$$

where ω_p is the plasma frequency, ω_r is the resonance frequency and F is the filling factor[20]. Here, without loss of generality, the damping terms are not considered [25]. The field profile for transvers electric (TE) waves have the form $(H_x, E_y, H_z)e^{i(\omega t-kz)}$. To obtain the electromagnetic wave equation for the DNG-MTM, we first take the Maxwell field equations as

$$\nabla \times H = i\omega\varepsilon_{\circ}\varepsilon_{_{DNG}}(\omega)E \tag{3}$$

$$\nabla \times E = -i\omega\mu_{\circ}\mu_{_{DNG}}(\omega)H \tag{4}$$

For the case of TE wave mode, Equations (3) and (4) have been used to obtain the following wave equation for E_y:

$$\frac{d^2E_y}{dx^2} + k_{\circ}^2\varepsilon_{_{DNG}}(\omega)E_y - k^2E_y = 0 \tag{5}$$

where $K_{\circ}^2 = \frac{\omega^2}{c^2}$. The solution of the above wave equation is given by

$$E_y = c_1 \sin k_{_{DNG}}\, x + c_2 \cos k_{_{DNG}}\, x \tag{6}$$

Here $k_{_{DNG}} = \left[k_{\circ}^2\varepsilon_{_{DNG}}(\omega)\mu_{_{DNG}}(\omega) - k^2\right]^{1/2}$. c_1 and c_2 are arbitrary constants and can be evaluated from the boundary conditions. Solution in Eq. (4) is used in Equation (4) to derive the following field components for TE-mode:

$$H_x = \frac{-k}{\omega\mu_{_{DNG}}(\omega)\mu_{\circ}}(c_1 \sin k_{_{DNG}}x + c_2 \cos k_{_{DNG}}x) \tag{7}$$

$$H_z = \frac{ik_{_{DNG}}}{\omega\mu_{_{DNG}}(\omega)\mu_{\circ}}(c_1 \cos k_{_{DNG}}x - c_2 \sin k_{_{DNG}}x) \tag{8}$$

A similar mathematical treatment can be performed to derive the wave equation in H_y for TM-mode to obtain the following solution:

$$H_y = c_3 \sin k_{_{DNG}}x + c_4 \cos k_{_{DNG}}x \tag{9}$$

where c_3 and c_4 are arbitrary constants and can be evaluated from the boundary conditions. Solution in Equation (9) is used in Equation (9) to derive the following field components for TE-mode:

$$E_x = \frac{-k}{\omega\varepsilon_{\circ}\varepsilon_{_{DNG}}(\omega)}(c_3 \sin k_{_{DNG}}x + c_4 \cos k_{_{DNG}}x) \tag{10}$$

$$E_z = \frac{ik_{_{DNG}}}{\omega\varepsilon_{\circ}\varepsilon_{_{DNG}}(\omega)}(c_3 \cos k_{_{DNG}}x + c_4 \sin k_{_{DNG}}x) \tag{11}$$

2.1. The dispersion relation

To find the dispersion relation for the TE and TM waves, we employ the following boundary conditions for the continuity on the field components at $x = 0$:

$$\text{TE Waves} : \begin{cases} E_y|_{x=0} \\ E_y|_{x=d} \end{cases} \tag{12}$$

$$\text{TM Waves} : \begin{cases} H_y|_{x=0} \\ H_y|_{x=d} \end{cases} \tag{13}$$

Using the values of E_y from Eq. (6) to Eq. (12), we obtain the following dispersion relation for TE mode:

$$k^2 = k_\circ^2 \varepsilon_{DNG}(\omega)\mu_{DNG}(\omega) - n^2\pi^2/a^2 \tag{14}$$

where $n = 1, 2, 3, \ldots$, known as number of modes. Similarly, using the values of H_y from Eq. (9) to Eq. (13), we obtain the dispersion relation for TM-mode which is exactly the same as given in Eq. (14).

2.2. Case of MNG-MTM

For the case of a PPWG loaded with MNG-MTM, we consider positive value of nonlinear permittivity i.e. ε_{MNG} (not a function of frequency) and frequency dependent negative permeability $\mu_{MNG}(\omega) = 1 - \omega_{mp}^2/\omega^2$, where ω_{mp} is the magnetic plasma frequency for MNG-MTM [26–28]. Therefore Eq. (5) can be written as

$$\frac{d^2E_y}{dx^2} + k_\circ^2 \varepsilon_{MNG}\mu_{MNG}(\omega)E_y - k^2E_y = 0 \tag{15}$$

and the solution of Eq. (6) becomes

$$E_y = c_5 \sin k_{MNG}x + c_6 \cos k_{MNG}x \tag{16}$$

where $k_{MNG} = \left[k_\circ^2 \varepsilon_{MNG}\mu_{MNG}(\omega) - k^2\right]^{1/2}$. The corresponding magnetic field components for TE-mode i.e. H_x and H_z are obtained from Eq. (4) and these are given by

$$H_x = \frac{-k}{\omega\mu_{MNG}(\omega)\mu_\circ}(c_5 \sin k_{MNG}x + c_6 \cos k_{MNG}x) \tag{17}$$

$$H_z = \frac{ik_{MNG}}{\omega\mu_{MNG}(\omega)\mu_\circ}(c_5 \cos k_{MNG}x + c_6 \sin k_{MNG}x) \tag{18}$$

Similarly, for TM-mode, the corresponding field components are given by

$$H_y = c_7 \sin k_{MNG}x + c_8 \cos k_{MNG}x \tag{19}$$

$$E_x = \frac{-k}{\omega\varepsilon_\circ\varepsilon_{MNG}}(c_7 \sin k_{MNG}x + c_8 \cos k_{MNG}x) \tag{20}$$

$$E_z = \frac{ik_{MNG}}{\omega\varepsilon_\circ\varepsilon_{MNG}}(c_7 \cos k_{MNG}x + c_8 \sin k_{MNG}x) \tag{21}$$

In this case, the following dispersion relation is obtained, for both TE and TM-modes, by applying the boundary conditions on Eq. (12) and (13) to Eqns. (16) and (19)

$$k^2 = k_\circ^2 \varepsilon_{MNG}\mu_{MNG}(\omega) - n^2\pi^2/a^2 \tag{22}$$

2.3. Case of ENG-MTM

For the case of PPWG loaded with an ENG-MTM, we consider frequency dependent negative permittivity i.e., $\varepsilon_{ENG}(\omega) = 1 - \omega_{ep}^2/\omega^2$, and a constant positive value of permeability μ_{ENG}, where ω_{ep} is the electron plasma frequency for ENG-MTM [26–28]. Therefore, Eq. (5) can be written as

$$\frac{d^2E_y}{dx^2} + k_\circ^2 \varepsilon_{ENG}(\omega)\mu_{ENG}E_y - k^2E_y = 0 \tag{23}$$

and the solution in Eq. (6) becomes

$$E_y = c_9 \sin k_{ENG}x + c_{10} \cos k_{ENG}x \tag{24}$$

where $k_{ENG} = \left[k_\circ^2 \varepsilon_{ENG}(\omega)\mu_{ENG} - k^2\right]^{1/2}$. The corresponding magnetic field components for TE-mode i.e., H_x and H_z are obtained from Eq. (4) and these are given by

$$H_x = \frac{-k}{\omega\mu_{ENG}\mu_\circ}(c_9 \sin k_{ENG}x + c_{10} \cos k_{ENG}x) \tag{25}$$

$$H_z = \frac{ik_{ENG}}{\omega\mu_{ENG}\mu_\circ}(c_9 \cos k_{ENG}x + c_{10} \sin k_{ENG}x) \tag{26}$$

Similarly, for TM-mode, the corresponding field components are given by

$$H_y = c_{11} \sin k_{ENG} + c_{12} \cos k_{ENG}x \tag{27}$$

$$E_x = \frac{-k}{\omega\varepsilon_\circ\varepsilon_{ENG}(\omega)}(c_{11} \sin k_{ENG}x + c_{12} \cos k_{ENG}x) \tag{28}$$

$$E_z = \frac{ik_{ENG}}{\omega\varepsilon_\circ\varepsilon_{ENG}(\omega)}(c_{11} \cos k_{ENG}x + c_{12} \sin k_{ENG}x) \tag{29}$$

In this case, the following dispersion relation is obtained, for both TE and TM-modes, by applying the boundary conditions on Eq. (12) and (13) to Eqns. (24) and (27)

$$k^2 = k_\circ^2 \varepsilon_{ENG}\mu_{ENG}(\omega) - n^2\pi^2/a^2 \tag{30}$$

2.4. Case of conventional PPWG

For the case of PPWG loaded with a conventional dielectric material, the permittivity and permeability have constant values i.e., ε_c and μ_c. Therefore, Eq. (5) can be written as

$$\frac{d^2E_y}{dx^2} + k_\circ^2 \varepsilon_{ENG}(\omega)\mu_{ENG}E_y - k^2E_y = 0 \tag{31}$$

and the solution of Eq. (6) becomes

$$E_y = c_{13} \sin k_c x + c_{14} \cos k_c x \tag{32}$$

where $k_c = \left[k_\circ^2 \varepsilon_c\mu_c - k^2\right]^{1/2}$. The corresponding magnetic field components for TE-mode i.e. H_x and H_z are obtained from Eq. (4) and these are given by

$$H_x = \frac{-k}{\omega\mu_c\mu_\circ}(c_{13} \sin k_c x + c_{14} \cos k_c x) \tag{33}$$

$$H_z = \frac{ik_c}{\omega\mu_c\mu_\circ}(c_{13} \cos k_c x - c_{14} \sin k_c x) \tag{34}$$

Similarly, for TM-mode, the corresponding field components are given by

$$H_y = c_{15} \sin k_c x + c_{16} \cos k_c x \tag{35}$$

$$E_x = \frac{-k}{\omega\varepsilon_\circ\varepsilon_c}(c_{15} \sin k_c x + c_{16} \cos k_c x) \tag{36}$$

$$E_z = \frac{ik_c}{\omega\varepsilon_\circ\varepsilon_c}(c_{15} \cos k_c x - c_{16} \sin k_c x) \tag{37}$$

In this case, the following dispersion relation is obtained, for both TE and TM-modes, by applying the boundary conditions in Eq. (12) and (13) to Eqns. (32) and (35)

$$k^2 = k_\circ^2 \varepsilon_c\mu_c - n^2\pi^2/a^2 \tag{38}$$

3. Numerical Analysis

In this section, we numerically analyze the dispersion relations by plotting the propagation constant against the frequency for the wave propagation in our proposed PPWGs. In this connection, we plot and discuss the dispersion diagrams for the TE and TM waves in both (i) conventional parallel-plate waveguide and (ii) parallel-plate waveguide filled with metamaterials. Before going into the details of the dispersion diagrams, first we have to find the frequency ranges in which (i) a DNG material has simultaneously negative values of permittivity and permeability (ii) an ENG material has negative value of permittivity (iii) a MNG material has negative value of permeability.

3.1. Frequency bands for metamaterials

To find the existence frequency bands for DNG and MNG-MTMs, we plot the permittivity and permeability of each material against the propagation frequency. In this connection, consider the relative permeability and permittivity for ENG-MTM as

$$\mu_{ENG} = 1.2\,, \qquad \varepsilon_{ENG} = 1 - \frac{\omega_{ep}^2}{\omega^2} \tag{39}$$

$$\varepsilon_{MNG} = 3\,, \qquad \varepsilon_{MNG} = 1 - \frac{\omega_{mp}^2}{\omega^2} \tag{40}$$

where, the parameter values chosen for both ω_{ep} and ω_{mp} is 10 GHz [26]. Further, for the DNG-MTM, we plot Eq. (1) and (2) for the parameters $F = 0.56$,$\omega_r = 4\times10^9$Hz and $\omega_p = 10\times10^9$ Hz [20, 29]. Fig. 2 shows a plot of permittivity and permeability versus the propagation frequency for a DNG-MTM. The graph shows that the frequency range in which both permittivity and permeability have simultaneously negative values extends from 4×10^9 Hz to 6×10^9 Hz, called frequency band for the existence of a DNG-MTM. Fig. 3 shows a plot of permittivity and permeability versus the propagation frequency for an ENG-MTM. The graph shows that the frequency range in which permittivity has negative value extends from 2.75×10^9 Hz to 12×10^9 Hz, called frequency band for the existence of an ENG-MTM. Fig. 4 shows a plot of permittivity and permeability versus the propagation frequency for a MNG-MTM. The graph shows that the frequency range in which permeability has negative value extends from 3.5×10^9 Hz to 10×10^9 Hz, called frequency band for the existence of an MNG-MTM.

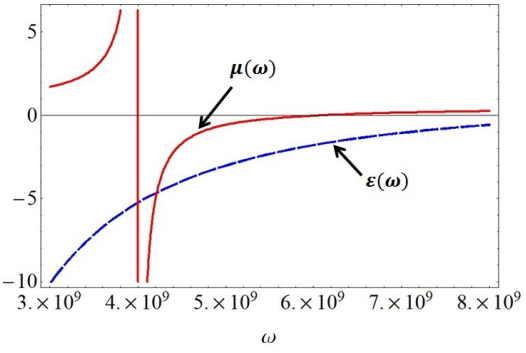

Figure 2: Plot of permittivity/permeability and frequency for a DNG-MTM

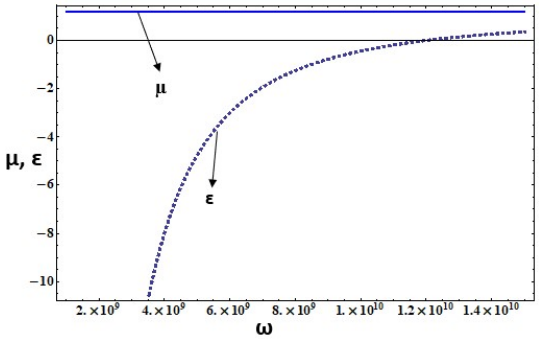

Figure 3: Plot of permittivity/permeability and frequency for a ENG-MTM

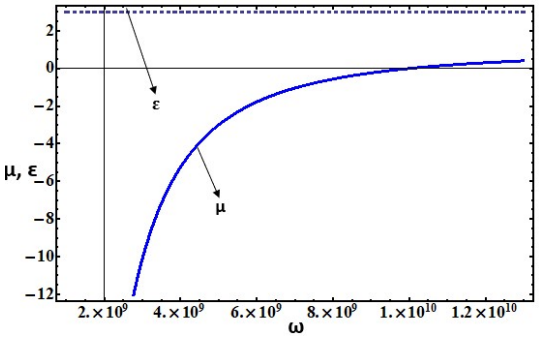

Figure 4: Plot of permittivity/permeability and frequency for a DNG-MTM

3.2. Dispersion characteristics

Table (1) shows the propagation conditions for the various materials used in our proposed PPWG. Case (a) shows that the permittivity and permeability of the medium is positive and therefore defines a right-handed or double positive material. For this case, the range of frequency considered to be in the microwave range from 109 Hz to 1012 Hz. In this case, the dispersion relation is $k = \sqrt{k_\circ^2\varepsilon_c\mu_c - n^2\pi^2/a^2}$ as given in Eq. (38). Here, k is real for $k_\circ^2\varepsilon_c\mu_c > \left(\frac{n\pi}{a}\right)^2$ which represents the propagation of electromagnetic waves, whereas k is imaginary for $k_\circ^2\varepsilon_r(\omega)\mu_r(\omega) < n^2\pi^2/a^2$, which represents the non-propagation of electromagnetic waves. Therefore, we can define a cut-off frequency separating the frequency band into propagation and non-propagation regions, i.e., $k_\circ^2\varepsilon_c\mu_c = n^2\pi^2/a^2$ for $\omega = \omega_c$, $k_\circ^2\varepsilon_c\mu_c > n^2\pi^2/a^2$ for $\omega > \omega_c$, and $k_\circ^2\varepsilon_c\mu_c < \pi^2/a^2$ for $\omega < \omega_c$, where $\omega_c = cn\pi/a\sqrt{\varepsilon_c\mu_c}$ is the cut-off frequency.

Fig. 5 shows a plot of dispersion relation (38) for k versus ω for a fix value of waveguide dimension (i.e., $a = 3\times10^{-3}$ m) and for different number of modes (i.e., $n = 1, 2, 3, \ldots$). This graph shows that the propagation region of the electromagnetic waves is above a certain frequency (i.e. cut-off frequency) for each mode. The propagation characteristics are sensitive to the

Table 1: Different cases for the permittivity and permeability of the Metamaterial

Cases	Permittivity $\varepsilon_r(\omega)$	Permeability $\mu_r(\omega)$	Product $\varepsilon_r(\omega)\mu_r(\omega)$	Range	Propagation	Non-propagation
a	$\varepsilon_r(\omega) > 0$	$\mu_r(\omega) > 0$	$\varepsilon_r(\omega)\mu_r(\omega) > 0$	$10^9 - 10^{12}$	$\omega > \omega_c$	$\omega < \omega_c$
b	$\varepsilon_r(\omega) > 0$	$\mu_r(\omega) < 0$	$\varepsilon_r(\omega)\mu_r(\omega) < 0$	$3.5 \times 10^9 - 10 \times 10^9$	Never	-
c	$\varepsilon_r(\omega) < 0$	$\mu_r(\omega) > 0$	$\varepsilon_r(\omega)\mu_r(\omega) < 0$	$2.75 \times 10^9 - 12 \times 10^9$	Never	-
d	$\varepsilon_r(\omega) < 0$	$\mu_r(\omega) < 0$	$\varepsilon_r(\omega)\mu_r(\omega) > 0$	$4 \times 10^9 - 6 \times 10^9$	Never	-

number of modes. The waveguide shows propagation in the upper region of the microwave band and there is no propagation for the lower region of the microwave band. Therefore, the parallel-plate waveguide filled with a double positive material (DPS-MTM) can be used as a high-pass filter etc.

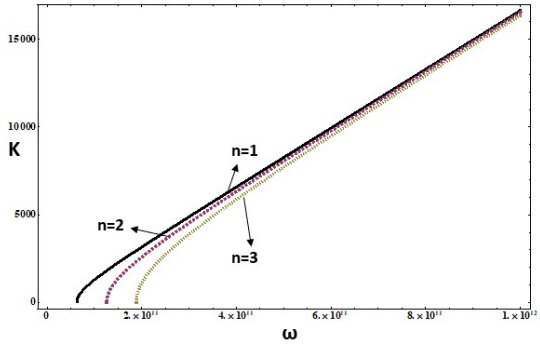

Figure 5: Dispersion diagram i.e. a plot of ω versus k for separation $a = 3 \times 10^{-3}$ m and for number of modes $n = 1, 2, 3$.

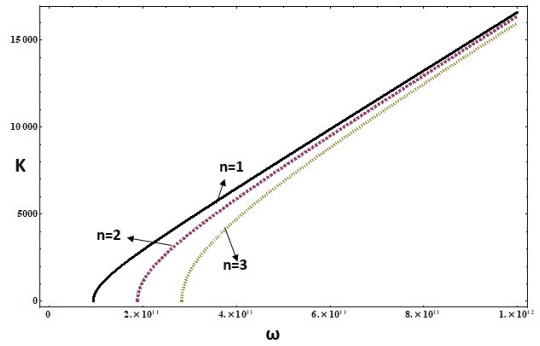

Figure 6: Dispersion diagram for separation $a = 2 \times 10^{-3}$ m and for number of modes $n = 1, 2, 3$. equation

Fig. 6 shows a plot of dispersion relation (38) for k versus ω for a fix value of plate separation (i.e., $a = 2 \times 10^{-3}$m) and for different number of modes (i.e., $n = 1, 2, 3, \ldots$). This graph shows the similar trends as discussed for Fig. 5. But here, the propagation characteristics are more sensitive to the number of modes. Further, the cut-off frequency for each mode is also different from the Fig. 5. The waveguide shows propagation in the upper region of the microwave band (i.e. from 109 Hz to 1012 Hz) and there is no propagation for the lower region of

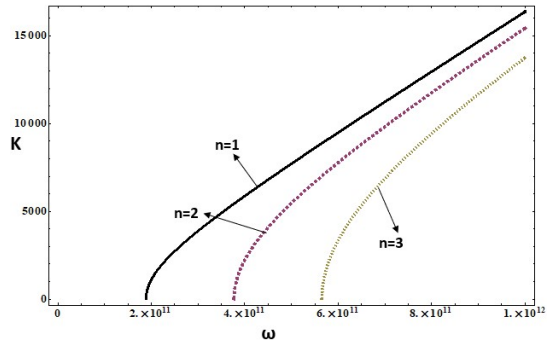

Figure 7: Dispersion diagram for separation $a = \times 10^{-3}$ m and for number of modes $n = 1, 2, 3$.

the microwave band. Same is the case with Fig. 7, which is a plot of dispersion relation (38) for k versus ω for a fix value of plate separation (i.e., $a = 10^{-3}$ m) and for different number of modes (i.e. $n = 1, 2, 3, \ldots$). This graph shows the similar trends as discussed for Fig. 5 and 6. But here again, the propagation characteristics are more sensitive to the number of modes. Further, the cut-off frequency for each mode is also different from the Fig. 5 and 6. The waveguide shows propagation in the upper region of the microwave band (i.e. from 109 Hz to 1012 Hz) and there is no propagation for the lower region of the microwave band. Therefore, one can choose the thickness to use the parallel-plate waveguide for the particular choice of high pass filter etc.

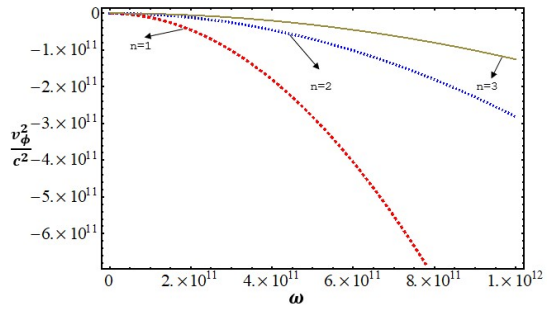

Figure 8: Dispersion diagram of v_{φ^2/c^2} versus ω for separation $a = 3 \times 10^{-3}$ m and for number of modes $n = 1, 2, 3$.

Case (b) and (c) show the propagation properties of the electromagnetic waves in MNG-MTM and ENG-MTM, respectively. Since, for an MNG-MTM, $\varepsilon_{MNG} > 0$ and $\mu_{MNG}(\omega) < 0$,

for which $\varepsilon_{MNG}\mu_{MNG}(\omega) < 0$, therefore, in the dispersion relation, $k = \sqrt{k_\circ^2\varepsilon_{MNG}\mu_{MNG}(\omega) - n^2\pi^2/a^2}$, k is always imaginary for this region within the frequency band of an MNG-MTM. Hence, electromagnetic waves cannot propagate in a parallel-plate waveguide filled with an MNG-MTM. Similarly, for an ENG-MTM, $\varepsilon_{ENG}(\omega) < 0$ and $\mu_{ENG} > 0$, for which $\varepsilon_{ENG}(\omega)\mu_{ENG} < 0$, so, in the dispersion relation, $k = \sqrt{k_\circ^2\varepsilon_{ENG}\mu_{ENG}(\omega) - n^2\pi^2/a^2}$, k is always imaginary for this region within the frequency band of an ENG-MTM. Hence, electromagnetic waves cannot propagate in a parallel-plate waveguide filled with an ENG-MTM.

Case (d) represents the propagation characteristics of the electromagnetic waves in DNG-MTM Since, for a DNG-MTM, $\varepsilon_{DNG}(\omega) < 0$ and $\mu_{DNG}(\omega) < 0$ for which $\varepsilon_{DNG}(\omega)\mu_{DNG}(\omega) > 0$. In dispersion relation, $k = \sqrt{k_\circ^2\varepsilon_{DNG}\mu_{DNG}(\omega) - n^2\pi^2/a^2}$, the frequency at which propagation may occur, does not exist in the existence band of a DNG-MTM (i.e., 4×10^9 Hz to 6×10^9 Hz) for the value of PPWG thicknesses $a < 10$mm. For the frequency range of simultaneous negative values of permittivity and permeability, the dispersion relation (14) does not show the region of propagation for different values of PPWG thickness a and for different values of modes n. Hence, electromagnetic waves cannot propagate in a parallel-plate waveguide filled with a DNG-MTM with the mentioned parameters. To show this finding, we present a graph of dispersion relation (14) for the normalized squared phase velocity v_φ^2/c^2 against the propagation frequency ω, within the frequency band of a DNG-MTM i.e., from 4×10^9 Hz to 6×10^9 Hz, as shown in Fig. 8. To show the non-propagation region in this graph, we write the dispersion relation (14) in the form of v_φ^2/c^2 as

$$\frac{v_\varphi^2}{c^2} = \left\{\varepsilon_{DNG}(\omega)\mu_{DNG}(\omega) - (cn\pi/\omega a)^2\right\}^{-1} \tag{41}$$

where, v_φ^2 is the square of phase velocity and c is the speed of light in vacuum. Fig. 8 is a plot of dispersion relation (14) for normalized squared phase velocity $\frac{v_\varphi^2}{c^2}$ versus ω for a fix value of plate separation (i.e., $a = 3\times10^{-3}$ m) and for different number of modes (i.e., $n = 1, 2, 3, \ldots$). The graph shows that the $\frac{v_\varphi^2}{c^2} < 0$ for the whole frequency band of a DNG-MTM, therefore, electromagnetic waves cannot propagate in a parallel-plate waveguide filled with a DNG-MTM.

4. Conclusion

In this research work, we analyze the electromagnetic wave propagation in a parallel-plate waveguide filled with a (a) conventional (linear, homogeneous and isotropic) dielectric medium (b) metamaterials. In this connection, we derived the field vectors and dispersion relations for the TE and TM wave modes for both cases. The dispersion characteristics of the waves are obtained by the numerical analysis of the dispersion relation. It is seen from the graph between permittivity and permeability versus the propagation frequency that the frequency band for the existence of ENG-MTM exists between 2.75×10^9 Hz and 12×10^9 Hz .The frequency range for DNG-MTM in which both permittivity and permeability have simultaneously negative values exists between 4×10^9 Hz and 6×10^9 Hz. Further, The frequency band for the existence of MNG-MTM is between 3.5×10^9 Hz and 10×10^9 Hz.

For a PPWG filled with a conventional dielectric medium, the dispersion curves show propagation of electromagnetic waves in upper region of microwave band but no propagation is seen in lower region within the microwave frequency range. Further, for a PPWG filled with a conventional dielectric medium, increasing the thickness between the plates of parallel-plate waveguide the propagation of electromagnetic waves also increases and vice versa. It is concluded that the propagation characteristics of electromagnetic are sensitive to the number of modes and the thickness of the waveguide. For a PPWG filled with a DNG-MTM, the frequency at which propagation may occur, does not exist in the existence band of a DNG-MTM for the value of PPWG thickness $a < 10mm$, whereas for very large plate separations, electromagnetic waves may propagate within the existence range of a DNG-MTM. Further, it is observed that electromagnetic waves cannot propagate in a parallel-plate waveguide filled with an MNG or ENG-MTM. Within the frequency bands for the existence of these MTMs, the dispersion relation does not show the region of propagation.

References

[1] N. Engheta, R. W. Ziolkowski, A positive future for double-negative metamaterials, IEEE Transactions on microwave theory and techniques 53 (4) (2005) 1535–1556.

[2] N. Engheta, R. W. Ziolkowski, Metamaterials: physics and engineering explorations, John Wiley & Sons, 2006.

[3] K. Y. Kim, Comparative analysis of guided modal properties of double-positive and double-negative metamaterial slab waveguides., Radioengineering 18 (2).

[4] M. Lapine, I. V. Shadrivov, Y. S. Kivshar, Colloquium: nonlinear metamaterials, Reviews of Modern Physics 86 (3) (2014) 1093.

[5] G. V. Eleftheriades, K. G. Balmain, Negative-refraction metamaterials: fundamental principles and applications, John Wiley & Sons, 2005.

[6] Y. Xiang, X. Dai, S. Wen, D. Fan, Properties of omnidirectional gap and defect mode of one-dimensional photonic crystal containing indefinite metamaterials with a hyperbolic dispersion, Journal of Applied Physics 102 (9) (2007) 093107.

[7] Y. Xiang, X. Dai, S. Wen, Omnidirectional gaps of one-dimensional photonic crystals containing indefinite metamaterials, JOSA B 24 (9) (2007) 2033–2039.

[8] W. Zhang, Y. Chen, P. Hou, J. Shi, Q. Wang, Transformation of nonlinear behaviors: from bright-to dark-gap soliton in a one-dimensional photonic crystal containing a nonlinear indefinite metamaterial defect, Physical Review E 82 (6) (2010) 066601.

[9] J. Yao, X. Yang, X. Yin, G. Bartal, X. Zhang, Three-dimensional nanometer-scale optical cavities of indefinite medium, Proceedings of the National Academy of Sciences 108 (28) (2011) 11327–11331.

[10] K. Kim, Y. Cho, Comparing guided modal properties of surface waves along single-and double-negative indexed slab waveguides, Opto-Electronics Review 18 (2010) 388–393.

[11] Y. Xiang, X. Dai, S. Wen, Negative and positive goos–hänchen shifts of a light beam transmitted from an indefinite medium slab, Applied Physics A 87 (2007) 285–290.

[12] Y. Xiang, X. Dai, J. Guo, H. Zhang, S. Wen, D. Tang, Critical coupling with graphene-based hyperbolic metamaterials, Scientific reports 4 (1) (2014) 5483.

[13] Y. Xiang, X. Dai, S. Wen, D. Fan, Independently tunable omnidirectional multichannel filters based on the fractal multilayers containing negative-index materials, Optics letters 33 (11) (2008) 1255–1257.

[14] Y. Xiang, J. Guo, X. Dai, S. Wen, D. Tang, Engineered surface bloch waves in graphene-based hyperbolic metamaterials, Optics Express 22 (3) (2014) 3054–3062.
[15] Y. G. Smirnov, D. V. Valovik, Guided electromagnetic waves propagating in a plane dielectric waveguide with nonlinear permittivity, Physical Review A 91 (1) (2015) 013840.
[16] V. G. Veselago, The electrodynamics of substances with simultaneously negative values of ε and μ, Soviet Physics Uspekhi 10 (4) (1968) 509.
[17] J. B. Pendry, A. Holden, W. Stewart, I. Youngs, Extremely low frequency plasmons in metallic mesostructures, Physical review letters 76 (25) (1996) 4773.
[18] J. B. Pendry, A. Holden, D. Robbins, W. Stewart, Low frequency plasmons in thin-wire structures, Journal of Physics: Condensed Matter 10 (22) (1998) 4785.
[19] J. B. Pendry, A. J. Holden, D. J. Robbins, W. Stewart, Magnetism from conductors and enhanced nonlinear phenomena, IEEE transactions on microwave theory and techniques 47 (11) (1999) 2075–2084.
[20] D. R. Smith, W. J. Padilla, D. Vier, S. C. Nemat-Nasser, S. Schultz, Composite medium with simultaneously negative permeability and permittivity, Physical review letters 84 (18) (2000) 4184.
[21] R. A. Shelby, D. R. Smith, S. Schultz, Experimental verification of a negative index of refraction, science 292 (5514) (2001) 77–79.
[22] A. Alù, N. Engheta, Guided modes in a waveguide filled with a pair of single-negative (sng), double-negative (dng), and/or double-positive (dps) layers, IEEE Transactions on Microwave Theory and Techniques 52 (1) (2004) 199–210.
[23] H. Jiang, H. Chen, H. Li, Y. Zhang, J. Zi, S. Zhu, Properties of one-dimensional photonic crystals containing single-negative materials, Phys. Rev. E 69 (2004) 066607.
[24] B. Zamir, R. Ali, Wave propagation in parallel-plate waveguides filled with nonlinear left-handed material, Chinese Physics B 20 (1) (2011) 014102.
[25] M. Shen, S. Pang, J. Zheng, J. Shi, Q. Wang, Nonlinear surface polaritons in indefinite media, JOSA B 29 (2) (2012) 197–202.
[26] S. R. Entezar, Frequency tuneable single-negative bistable heterostructure, Progress In Electromagnetics Research M 14 (2010) 33–44.
[27] W.-H. Lin, C.-J. Wu, S.-J. Chang, Angular dependence of wave reflection in a lossy single-negative bilayer, Progress In Electromagnetics Research 107 (2010) 253–267.
[28] A. Namdar, S. R. Entezar, H. Rahimi, H. Tajalli, Backward tamm states in 1d single-negtaive metamaterials photonic crystals, Progress In Electromagnetics Research Letters 13 (2010) 149–1159.
[29] I. V. Shadrivov, A. A. Sukhorukov, Y. S. Kivshar, A. A. Zharov, A. D. Boardman, P. Egan, Nonlinear surface waves in left-handed materials, Physical Review E 69 (1) (2004) 016617.

RPNS is a biannual scholarly periodical published by Govt Graduate College Township, Lahore, that strives to disseminate the empirical work of researchers worldwide through scrutinized research articles, with the intention of establishing itself as a leading forum for top-notch research publications and endorsing learned treatises and research papers.